The Effects of Uncorrelated Measurement Noise on SWOT Estimates of Sea Surface Height, Velocity, and Vorticity

Dudley B. Chelton,[a] Roger M. Samelson,[a] and J. Thomas Farrar[b]

[a] *College of Earth, Ocean and Atmospheric Sciences, Oregon State University, Corvallis, Oregon*
[b] *Woods Hole Oceanographic Institution, Woods Hole, Massachusetts*

ABSTRACT: The Ka-band Radar Interferometer (KaRIn) on the Surface Water and Ocean Topography (SWOT) satellite will revolutionize satellite altimetry by measuring sea surface height (SSH) with unprecedented accuracy and resolution across two 50-km swaths separated by a 20-km gap. The original plan to provide an SSH product with a footprint diameter of 1 km has changed to providing two SSH data products with footprint diameters of 0.5 and 2 km. The swath-averaged standard deviations and wavenumber spectra of the uncorrelated measurement errors for these footprints are derived from the SWOT science requirements that are expressed in terms of the wavenumber spectrum of SSH after smoothing with a filter cutoff wavelength of 15 km. The availability of two-dimensional fields of SSH within the measurement swaths will provide the first spaceborne estimates of instantaneous surface velocity and vorticity through the geostrophic equations. The swath-averaged standard deviations of the noise in estimates of velocity and vorticity derived by propagation of the uncorrelated SSH measurement noise through the finite difference approximations of the derivatives are shown to be too large for the SWOT data products to be used directly in most applications, even for the coarsest footprint diameter of 2 km. It is shown from wavenumber spectra and maps constructed from simulated SWOT data that additional smoothing will be required for most applications of SWOT estimates of velocity and vorticity. Equations are presented for the swath-averaged standard deviations and wavenumber spectra of residual noise in SSH and geostrophically computed velocity and vorticity after isotropic two-dimensional smoothing for any user-defined smoother and filter cutoff wavelength of the smoothing.

KEYWORDS: Sea level; Altimetry; Remote sensing; Satellite observations; Error analysis

1. Introduction

Presently available sea surface height (SSH) fields constructed from measurements by multiple nadir-viewing satellite altimeters are able to resolve midlatitude variability on wavelength scales down to about 200 km and monthly time scales (Chelton et al. 2011; Ballarotta et al. 2019). This resolution capability will soon be greatly improved by SSH measurements from the Surface Water and Ocean Topography (SWOT) satellite (Fu and Ferrari 2008; Durand et al. 2010; Fu and Ubelmann 2014) that has a target launch date in November 2022. The primary instrument on SWOT is the Ka-band Radar Interferometer (KaRIn) that will determine SSH from measurements at a microwave frequency of 35.75 GHz using radar interferometry and synthetic aperture radar technology (see appendix B; see also Fu and Rodríguez 2004). KaRIn will estimate SSH with a footprint diameter of order 1 km across a pair of swaths 50 km wide separated by a 20-km gap centered on the satellite ground track. The high accuracy and spatial resolution of the KaRIn data and the wide KaRIn measurement swath will significantly improve the space–time resolution capability of SSH fields. This will greatly benefit studies of mesoscale ocean dynamics. Among other applications, the smaller errors in maps of SSH constructed from

SWOT data will reduce the mislocations of mesoscale eddies in presently available SSH fields (e.g., Pascual et al. 2006). The innovative measurements of SSH by KaRIn will also provide insight into ocean dynamics in the submesoscale regime, and the role of these small scales in influencing or connecting to the dynamics at larger scales.

While the primary goal of the SWOT mission is to improve the present SSH mapping capabilities, SWOT will also enable the first spaceborne estimates of instantaneous surface vector velocity and relative vorticity (referred to hereinafter as vorticity) that can be computed geostrophically from the gridded SSH fields within the two SWOT measurement swaths. Estimates of these variables from the SSH fields constructed from merged multimission altimeter data are limited by the above-noted 200-km wavelength and monthly time-scale resolution of these SSH fields. Surface vector velocity can be estimated geostrophically from a single nadir-viewing altimeter on the coarse grid of crossovers of ascending and descending ground tracks. However, in addition to the effects of SSH measurement noise on errors in the geostrophically computed across-track velocities, the accuracies of the vector velocity estimates at the crossovers are limited by sampling errors from nonsimultaneity of the ascending and descending overpasses and errors from the geometrical transformation of the two across-track velocity estimates that are in general nonorthogonal at the crossovers. The sampling errors and geometrical transformation errors both vary latitudinally because of latitudinal variations of the time separation and angle between ascending and descending ground tracks (Schlax and Chelton 2003).

The ability to estimate vector velocity and vorticity instantaneously by altimetry is thus unique to the gridded SSH estimates across the two parallel KaRIn measurement swaths. Although the SWOT mission was not designed to determine the surface velocity and vorticity fields, many researchers intend to investigate ocean dynamics from SWOT estimates of these variables. The equations from which the standard deviations and wavenumber spectra of noise can be computed for all of the variables of interest (SSH, geostrophically computed velocity components u_g and v_g, and the vorticity ζ_g) are presented in this study for any choice of footprint diameter in the ground-based processing and subsequent additional spatial smoothing, referred to here as postprocessing.

Our reference to u_g and v_g as "geostrophically computed velocity components" rather than "geostrophic velocity components" is deliberate. There are several reasons the pressure field might not be in geostrophic balance with the velocity field. For example, the geostrophic approximation is valid only for small Rossby number. Because of the high incidence of large Rossby numbers at small scales (see Figs. 4 and 5 of Chelton et al. 2019, referred to hereinafter as C19), the velocity components computed from the geostrophic equations (see appendix D) give velocity estimates that may not be truly geostrophic on all scales. A significant concern is the possibility of erroneous contributions to the computed velocity from gradients of the ageostrophic SSH signatures of internal tides and internal waves with short wavelengths that may be resolvable in the SWOT data. Because of the large degree of smoothing that will have to be applied in postprocessing to mitigate the effects of measurement noise on estimates of velocity and vorticity computed geostrophically from SWOT data (see sections 3–5), most of the ageostrophic signals will be attenuated by the filtering. We therefore neglect errors of the geostrophic approximation in the analysis that follows.

It is noteworthy that the surface velocity field on the large scales that are resolvable in SWOT data includes wind-driven Ekman currents. These large-scale ageostrophic contributions to velocity cannot be addressed from velocities computed geostrophically from SWOT data (Yu et al. 2021).

The SWOT satellite will also include a dual-frequency nadir altimeter that will measure SSH at Ku-band and C-band frequencies of 13.6 and 5.3 GHz with a footprint size and measurement precision that are very different from KaRIn. The footprint for 1-s averages of nadir altimeter measurements from the SWOT orbit altitude of 890 km for a significant wave height (SWH) of 2 m has across-track and along-track dimensions of approximately 3.5 km $\times$ 10 km (see Figs. 22 and 23 of Chelton et al. 2001). These footprint dimensions increase with increasing SWH. The nadir altimeter measurements are expected to have a noise standard deviation of 1.7 cm (see Table 5 of JPL 2017a). In comparison, the noise standard deviation of KaRIn measurements of SSH for a much smaller footprint diameter of 2 km is expected to be about 1.4 cm (see section 2 and appendix C). Because the precision and footprint size for KaRIn differ so much from those of the nadir altimeter, the latter is not considered in this study. Hereinafter, we will generally refer to SWOT estimates of

SSH with the implicit understanding that we consider only the estimates from KaRIn.

This study also considers only the effects of uncorrelated measurement errors (which we will refer to interchangeably as measurement noise) in KaRIn estimates of SSH and how they affect spatially smoothed estimates of instantaneous SSH as well as SWOT estimates of surface velocity and vorticity computed from instantaneous SSH for a chosen footprint diameter, both without additional smoothing and with spatial smoothing applied in postprocessing. The effects of long-wavelength measurement errors are not addressed in this study. Because of the high-pass filtering operation of the derivative operator, long-wavelength measurement errors have relatively little effect on SWOT estimates of velocity and vorticity. We also do not consider the sampling errors that arise from space–time smoothing of SWOT data from multiple overpasses of SWOT, which are addressed in section 8 of C19 and discussed briefly here in section 6.

The analysis in this study draws heavily from the appendixes of C19. The standard deviation σ_h of the uncorrelated noise in SWOT estimates of SSH depends on the chosen footprint diameter. Although σ_h for a specified footprint diameter is the fundamental characterization of the uncorrelated measurement errors, this information is difficult to find and ambiguous in the current versions of the SWOT documents. Furthermore, the footprint diameter of the SWOT estimates of SSH in the data products that will be provided by the SWOT Project Office has evolved from the original plan that was to provide only a single product with a footprint diameter of 1 km. The new plan is to provide two data products, one with a footprint diameter of 0.5 km and the other with a footprint diameter of 2 km. To date, the only documentations of this change are the recent SWOT Product Description Document (JPL 2020) and revision B of the Onboard Processing and Algorithm Theoretical Basis Document (JPL 2021). To the enlightened reader, hints of the change to footprint diameters of 0.5 and 2 km can be inferred from sections 2.7.1a and 2.7.1b of the current version of the Science Requirements Document (JPL 2018). The current version of the Mission Performance and Error Budget Document (JPL 2017a) describes only the original planned footprint diameter of 1 km.

An objective of this study is to present the equations for the standard deviations and along-track wavenumber spectra of the noise of all of the variables of interest (SSH, geostrophically computed velocity components, and vorticity) in terms of the standard deviation σ_h of SSH noise for each of the three footprint diameters of 0.5, 1, and 2 km. These equations are presented in a series of appendixes, beginning with a summary in appendix A of the science requirements for KaRIn. The requirement for the uncorrelated errors in KaRIn measurements of SSH that are the focus of this study are specified in a nonconventional manner in terms of the swath-averaged along-track wavenumber spectrum of the noise after smoothing the data with a half-power filter cutoff wavelength of 15 km. After an overview of the onboard and ground-based processing of SWOT data in appendix B, the swath-averaged standard deviations of the measurement noise in the SSH estimates without 15-km smoothing are derived in appendix C

from the spectral characterization for the three footprint diameters of 0.5, 1, and 2 km. Our analysis assumes that the spectral characteristics of uncorrelated measurement errors are "white" (i.e., constant) for all wavenumbers up to the Nyquist wavenumber of $(2\Delta y)^{-1}$ that is associated with an along-track sample grid spacing of Δy that is equal to the footprint diameter. Note, however, that the science requirements specify a white-noise spectrum only for wavenumbers up to 1/15 cycles per kilometer (cpkm), i.e., wavelengths longer than 15 km (see appendix A).

The equations for the swath-averaged standard deviations of the noise in velocity components computed from SSH by finite-difference approximations of the derivatives in the geostrophic equations, and of the noise in vorticity estimated from finite-difference approximations of the derivatives of the geostrophically computed velocity components, are presented in appendix D. The discussion in appendix D of the standard deviations of the noise in SWOT estimates of all three variables (SSH, velocity, and vorticity) is extended in appendix E to present equations for the along-track wavenumber spectral characteristics of the noise without 15-km smoothing.

As summarized in section 2, the conclusion from the analysis in appendixes D and E is that velocity and vorticity computed geostrophically from the SWOT SSH data products will be too noisy to be used directly for most applications, even for the coarsest footprint diameter of 2 km considered here. Most analyses of SWOT data over oceans will therefore be based on the 2-km SSH product provided by the SWOT Project, with additional smoothing applied in postprocessing to reduce the noise and improve the signal-to-noise ratio. The additional smoothing will be especially important for SWOT estimates of velocity and vorticity. The equations for the standard deviations and wavenumber spectra of the noise in smoothed SWOT estimates of all three variables are presented in sections 3 and 4.

Example maps of SSH and geostrophically computed velocity magnitude and vorticity constructed from simulated SWOT data are presented in section 5 for selected choices of smoothing in postprocessing. The simulated SWOT data include uncorrelated noise with the swath-averaged standard deviation σ_h derived in appendix C for the footprint diameter of 2 km that will likely be the SWOT data product preferred by most users. The purpose of presenting these maps is to provide a visual sense of what to expect from SWOT data with various amounts of smoothing applied in postprocessing. The maps also provide insight into the contamination that can be expected from edge effects of smoothing within the 50-km width of the two measurement swaths.

For easy application, the equations in appendixes C–E and sections 3 and 4 are all expressed in terms of the across-track and along-track grid spacings Δx and Δy and standard deviation σ_h of the SWOT data product with the specified footprint diameter. The table and figures presented in this study are based on the prelaunch estimates of σ_h that are derived in appendix C for the footprint diameters of 0.5, 1, and 2 km. The SSH noise standard deviation σ_h that appears in the equations from which the table and figures were generated can be replaced with the actual value determined after launch

from in-orbit data for any specified footprint diameter, grid spacing of the data, swath location, and significant wave height. Moreover, the equations presented here will be applicable to future versions of the SWOT data products in which the measurement noise standard deviations σ_h are likely to decrease through improvements in the onboard and ground-based processing of SWOT data.

2. The effects of uncorrelated measurement noise on "unsmoothed" SWOT estimates of SSH, velocity, and vorticity

The errors in SWOT estimates of SSH, velocity, and vorticity have previously been investigated by C19 for the case of a footprint diameter of 1 km that was the original plan for the gridded SWOT data product. As noted in the introduction, the SWOT Project has recently replaced the 1-km data product with two gridded SSH products with footprint diameters of 0.5 and 2 km. The error analysis in C19 is extended here in appendixes C–E to derive the standard deviations and wavenumber spectra of the noise for these new footprint diameters. We refer to SWOT estimates of SSH, velocity, and vorticity with a chosen footprint diameter as "unsmoothed." In actuality, they are produced by two-dimensional smoothing of the raw SWOT data that have a resolution of tens of meters (see appendix B) using a filter that has a half-power filter cutoff wavelength of approximately twice the footprint diameter (see appendix B.1 of C19). SWOT estimates of SSH, velocity, and vorticity generated from SWOT data with any of the three footprint diameters considered in this study are referred to as "smoothed" when they are subsequently filtered in postprocessing to improve the signal-to-noise ratio by reducing the small-scale noise.

Expressions for the standard deviations of the noise in unsmoothed SWOT estimates of SSH, the geostrophically computed velocity components u_g and v_g, and the vorticity ζ_g computed from u_g and v_g are presented in appendixes C and D for each of the three footprint diameters of 0.5, 1, and 2 km. The results are summarized in the top half of Table 1. The noise standard deviation for SWOT measurements of SSH with a footprint diameter of 2 km that is the data product likely to be preferred by most users is 1.37 cm. As noted in the introduction, this is smaller than the noise deviation of about 1.7 cm in SSH measurements from conventional nadir altimeters with their much larger footprint dimensions. The noise standard deviations for SWOT estimates of velocity components and vorticity are comparable to or larger than the signal standard deviations in most regions of the World Ocean for all three footprint diameters considered here. The challenges of distinguishing signal and noise are further underscored in appendix E by the wavenumber spectra of unsmoothed SWOT estimates of velocity and vorticity that are shown to be more energetic than the signal spectra over most wavenumbers (see Fig. E1).

The conclusions from the analysis in appendixes C–E and the noise statistics summarized in the top half of Table 1 and in Fig. E1 are thus that SWOT data will have to be smoothed in postprocessing for most ocean applications in order to

TABLE 1. The swath-averaged standard deviations of the noise in SWOT estimates of SSH, geostrophically computed velocity components u_g and v_g and relative vorticity ζ_g. The top half of the table lists the noise standard deviations for "unsmoothed" data with footprint diameters of 0.5, 1.0, and 2.0 km. Results for the case of 0.5-km footprint diameter are shown for a sample grid spacing of 0.5 km × 0.5 km on which the measurement errors are uncorrelated, and on an oversampled grid spacing of 0.25 km × 0.25 km. The bottom half of the table lists the residual noise standard deviations for the case of 2-km footprint diameter after additional smoothing in postprocessing using a Parzen smoother with selected half-power filter cutoff wavelengths. The geostrophic calculations are based on a Coriolis parameter of $f_{37°N} = 8.75 \times 10^{-5}$ s^{-1} at the central latitude 37°N of the model of the California Current System used here (see Fig. 3). The noise in u_g and v_g for other latitudes can be determined by multiplying the values in the fourth column by $f_{37°N}/f$, where f is the magnitude of the Coriolis parameter at the latitude of interest. The noise of ζ_g/f can be determined by multiplying the values in the last column by $(f_{37°N}/f)^2$.

Footprint diameter (km)	Grid spacing (km)	σ_h (cm)	σ_{u_g}, σ_{v_g} at 37°N (m s^{-1})	σ_{ζ_g} at 37°N (s^{-1})	σ_{ζ_g}/f at 37°N
			Unsmoothed noise		
0.5	0.25	5.48	16.99	1.05×10^{-1}	1198.1
0.5	0.5	5.48	8.67	2.74×10^{-2}	312.3
1.0	1.0	2.74	2.17	3.43×10^{-3}	39.0
2.0	2.0	1.37	0.54	4.28×10^{-4}	4.9
Filter cutoff (km)	Grid spacing (km)	σ_h (cm)	σ_{u_g}, σ_{v_g} at 37°N (m s^{-1})	σ_{ζ_g} at 37°N (s^{-1})	σ_{ζ_g}/f at 37°N
			Smoothed noise		
15	2.0	0.37	0.118	8.06×10^{-5}	0.920
30	2.0	0.19	0.034	1.51×10^{-5}	0.172
50	2.0	0.11	0.013	3.59×10^{-6}	0.041
70	2.0	0.08	0.007	1.34×10^{-6}	0.015

reduce the noise, especially for SWOT estimates of velocity and vorticity. Such smoothing attenuates the signal as well as the noise. The noise power is attenuated more than the signal power because the SSH, velocity, and vorticity signals are more dominated by spatially correlated low-wavenumber variability (see the thick black lines in Fig. E1). The signal-to-noise ratios therefore improve with increased smoothing. Estimation of ζ_g is the most challenging because the signal is less dominated by large-scale variability (see Fig. E1d) and is therefore more attenuated by the smoothing. The effects of smoothing on the standard deviation and wavenumber spectra of residual noise in SWOT estimates of SSH, velocity, and vorticity are quantified in sections 3 and 4.

3. The standard deviations of smoothed noise in SWOT estimates of SSH, velocity, and vorticity

The equations for the swath-averaged standard deviations of residual noise in SWOT estimates of SSH, u_g, v_g, and ζ_g after the two-dimensional smoothing in the postprocessing that will be required for most ocean applications of the SWOT data that will be provided by the SWOT Project are derived in appendix G.3 of C19. Our simulated postprocessing is based on isotropic two-dimensional smoothing using the Parzen smoother that is discussed in detail in appendix A of C19. The results would be very similar for other choices of smoother, as long as the parameters of the smoother are calibrated to give the same half-power filter cutoff wavelength λ_c. A useful characteristic of the Parzen smoother is that its filter transfer function is almost identical to that of a Gaussian smoother (see Fig. C2 in appendix C of C19). A convenient property of the Gaussian smoother is that isotropic two-dimensional smoothing that depends only on the radial distance of each data point from the estimation location can be

achieved equivalently through successive one-dimensional smoothing operations in each of two orthogonal dimensions. The similarity of the filter transfer functions of the Parzen and Gaussian smoothers implies that isotropic two-dimensional smoothing with the Parzen smoother can essentially be achieved equivalently with separate one-dimensional smoothing in two orthogonal dimensions. A distinct advantage of separate one-dimensional smoothing is that it facilitates the derivations of the analytical equations in section 4 below for the wavenumber spectra of residual noise in smoothed estimates of SSH, u_g, v_g, and ζ_g. While the Parzen smoother nearly replicates the exact equivalence of isotropic two-dimensional smoothing and sequential one-dimensional smoothing in two orthogonal dimensions for the Gaussian smoother, this equivalence is only approximate for most other smoothing algorithms.

To provide context for the analysis in this section, it is useful to display the noise standard deviations graphically for unsmoothed SWOT estimates of SSH, velocity, and vorticity as functions of the half-power filter cutoff wavelengths associated with each of the footprint diameters of 0.5, 1, and 2 km. It is shown in appendix B.1 of C19 that SSH estimates with a footprint diameter of 1 km can be achieved with isotropic two-dimensional smoothing of raw SWOT data using a Parzen smoother (see, however, the footnote in appendix B of this paper) with a half-power filter cutoff wavelength of 2 km, i.e., twice the desired footprint diameter. It is also shown in appendix B.1 of C19 that the noise in these estimates of SSH is uncorrelated on a grid spacing of 1 km × 1 km. SWOT estimates of SSH, velocity, and vorticity with the footprint diameters of 0.5 and 2 km can correspondingly be obtained by two-dimensional smoothing of raw SWOT data using Parzen smoothers with half-power filter cutoff wavelengths of 1 and 4 km, respectively, and the noise for these footprints is uncorrelated on grids with spacings equal to the

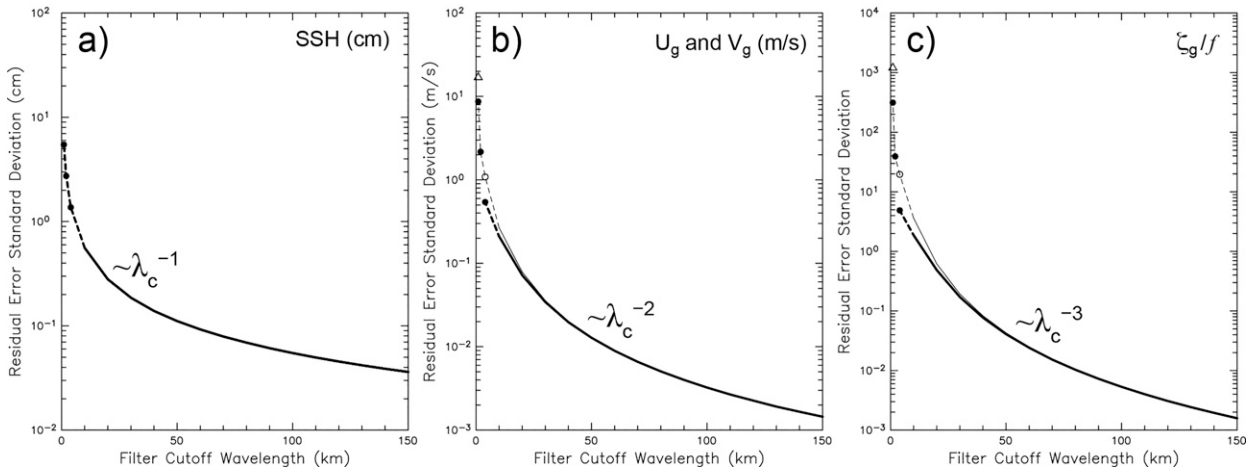## Standard Deviations of Smoothed SSH, Velocity and Vorticity Noise

FIG. 1. The standard deviations of residual noise as functions of half-power filter cutoff wavelength λ_c for isotropic two-dimensional smoothing of SWOT data with a Parzen smoother: (a) SSH, (b) velocity component estimates computed geostrophically from SSH based on the Coriolis parameter $f_{37°N} = 8.75 \times 10^{-5} \text{ s}^{-1}$ for a latitude of 37°N, and (c) vorticity computed from the geostrophic estimates of velocity and normalized by $f_{37°N}$. The three solid circles correspond to the error standard deviations for footprint diameters of 0.5, 1, and 2 km (filter cutoff wavelengths of 1, 2, and 4 km). The solid lines are the standard deviations of residual noise after smoothing for footprint diameters of 1 km on a 1 km × 1 km grid (thin lines) and 2 km on a 2 km × 2 km grid (thick lines). The open triangles in (b) and (c) are the noise standard deviations for a footprint diameter of 0.5 km on an oversampled 0.25 km × 0.25 km grid. The open circles in (b) and (c) are the standard deviations for a footprint diameter of 1 km on a 1 km × 1 km grid smoothed with the half-power filter cutoff wavelength of 4 km; these noise standard deviations are larger than for the footprint diameter of 2 km on a 2 km × 2 km grid because the finite differences are computed on a smaller grid spacing.

respective footprint diameters. (As discussed in appendixes B and C of this study, the SWOT Project may decide to smooth the SSH with a half-power filter cutoff wavelength somewhat longer than 4 km for the 2 km × 2 km data product; such increased smoothing would not significantly alter any of the conclusions of this study.)

The standard deviations listed in the top half of Table 1 for the SSH noise with the three footprint diameters of 0.5, 1, and 2 km and sample grid spacings equal to the footprint diameters (rows 2–4 in Table 1) are displayed at their associated filter cutoff wavelengths of 1, 2, and 4 km by the solid circles in Fig. 1a. The corresponding noise standard deviations for the geostrophically computed velocity components u_g and v_g and the vorticity ζ_g are shown by the solid circles in Figs. 1b and 1c. The noise standard deviation for SSH with the footprint diameter of 0.5 km is the same on the oversampled 0.25 km × 0.25 km grid as on the 0.5 km × 0.5 km grid. However, the noise standard deviations for u_g, v_g, and ζ_g with the footprint diameter of 0.5 km are larger on the oversampled 0.25 km × 0.25 km grid (see row 1 in Table 1 and the triangles in Figs. 1b and 1c). This is because the finite-difference approximations of the derivatives are computed on a smaller grid spacing, which increases the noise in accord with (D3), (D4), and (D7).

Because of the excessively large noise standard deviations for all three variables with the footprint diameter of 0.5 km, this case is not considered further in the discussion that follows. The standard deviations of the residual noise in SWOT estimates of SSH, u_g, v_g, and ζ_g after isotropic two-

dimensional smoothing in postprocessing are determined in this section only for the footprint diameters of 1 and 2 km.

The variance of the residual noise in SSH after isotropic two-dimensional smoothing in postprocessing, which will be denoted here with an overbar, can be expressed in terms of the variance σ_h^2 of unsmoothed SSH by Eq. (D.5a) in appendix D of C19, which is

$$\overline{\sigma}_h^2 = \alpha\, \sigma_h^2. \tag{1a}$$

For grid spacings Δx and Δy in the x and y dimensions and smoothing using a Parzen smoother with a half-power filter cutoff wavelength of λ_c in each of two orthogonal dimensions (which is essentially the same as isotropic two-dimensional smoothing with a Gaussian smoother, as discussed at the beginning of this section), the scaling factor α in (1a) is given by Eq. (D.14c) of C19, which is

$$\alpha \approx \frac{4\,\Delta x \Delta y}{\lambda_c^2}. \tag{1b}$$

Note that this expression is applicable only for a grid spacing $\Delta x \times \Delta y$ on which the measurement errors are uncorrelated. For the case of Δx and Δy equal to the footprint diameter, i.e., the minimum grid spacing on which the SSH measurement noise is uncorrelated, it is evident from (1a) and (1b) that $\overline{\sigma}_h^2$ for any specified λ_c is the same for any footprint diameter. This can be seen mathematically by noting that doubling the footprint diameter from 1 to 2 km, for example, reduces the

noise variance σ_h^2 on the right side of (1a) by a factor of 4 but doubles the sample spacings $\Delta x = \Delta y$ for uncorrelated noise in the numerator of (1b), thus increasing the product $\Delta x \Delta y$ by a factor of 4. The two factors of 4 cancel for any choice of filter cutoff wavelength λ_c. The variance of smoothed SSH is therefore independent of footprint diameter if the grid spacings Δx and Δy are chosen to be equal to the footprint diameter. The variance (1) of smoothed SSH noise is thus proportional to λ_c^{-2} so that the SSH noise standard deviation $\overline{\sigma}_h$ decreases as λ_c^{-1}. The resulting dependence of $\overline{\sigma}_h$ on λ_c is shown in Fig. 1a. The analytical expression for this curve obtained from (1a) and (1b) is

$$\overline{\sigma}_h = a_h \lambda_c^{-1}, \tag{2}$$

where $a_h = 5.48$ cm km. Note the relationship between a_h and the SSH measurement noise standard deviation of $\sigma_h = 5.48$ cm for a half-power filter cutoff wavelength of $\lambda_c = 1$ km, i.e., a footprint diameter of 0.5 km (see Table 1).

The variance of the residual noise in the geostrophically computed velocity component v_g after isotropic two-dimensional smoothing in postprocessing can be expressed in terms of the variance $\overline{\sigma}_h^2$ of the smoothed SSH measurement noise by Eq. (G.17a) of C19, which is

$$\overline{\sigma}_{v_g}^2 = \frac{g^2}{f^2}\frac{1}{2\Delta x^2}\big[1 - \overline{\rho}_h(2\Delta x)\big]\overline{\sigma}_h^2, \tag{3a}$$

where $\overline{\rho}_h(2\Delta x)$ is the autocorrelation of the smoothed estimates of SSH noise at an across-track lag of $2\Delta x$. Substituting (1) for $\overline{\sigma}_h^2$ expresses $\overline{\sigma}_{v_g}^2$ in terms of the variance σ_h^2 of unsmoothed SSH,

$$\overline{\sigma}_{v_g}^2 = \frac{g^2}{f^2}\frac{2\Delta y}{\lambda_c^2 \Delta x}\big[1 - \overline{\rho}_h(2\Delta x)\big]\sigma_h^2. \tag{3b}$$

The analogous expressions for the variance of the residual noise in the geostrophically computed velocity component u_g after isotropic two-dimensional smoothing in postprocessing are

$$\overline{\sigma}_{u_g}^2 = \frac{g^2}{f^2}\frac{1}{2\Delta y^2}\big[1 - \overline{\rho}_h(2\Delta y)\big]\overline{\sigma}_h^2 \tag{4a}$$

$$= \frac{g^2}{f^2}\frac{2\Delta x}{\lambda_c^2 \Delta y}\big[1 - \overline{\rho}_h(2\Delta y)\big]\sigma_h^2, \tag{4b}$$

where $\overline{\rho}_h(2\Delta y)$ is the autocorrelation of the smoothed estimates of SSH noise at an along-track lag of $2\Delta y$. For homogeneous noise and a uniform sample grid spacing $\Delta y = \Delta x$, the variances (3) and (4) of smoothed noise in v_g and u_g are the same.

The right sides of the forms (3a) and (4a) for the variances of smoothed estimates of v_g and u_g are the same as the right sides of the expressions (D3b) and (D4) for the variances of noise in unsmoothed v_g and u_g, except with overbars to indicate the variances and lagged autocorrelations of smoothed estimates. The lagged autocorrelations for smoothed SSH inside the square brackets in (3) and (4) are always larger than their counterpart lagged autocorrelations for unsmoothed SSH inside the square brackets in (D3b) and (D4). The forms

(3b) and (4b) for $\overline{\sigma}_{v_g}^2$ and $\overline{\sigma}_{u_g}^2$ allow calculation of the variances of the residual noise in smoothed geostrophically computed SWOT estimates of the velocity components for any choice of half-power filter cutoff wavelength λ_c from the variance σ_h^2 of the unsmoothed SSH noise for the footprint diameter of interest, the specified across-track and along-track grid spacings Δx and Δy, respectively, and the lagged autocorrelations $\overline{\rho}_h(2\Delta x)$ and $\overline{\rho}_h(2\Delta y)$ of the smoothed SSH for the particular choice of λ_c.

Some general comments can be made on the interpretations of (3) and (4). As discussed above from (1), the residual variance $\overline{\sigma}_h^2$ of the smoothed SSH noise is independent of footprint diameter for any specified filter cutoff wavelength λ_c when the grid spacings are chosen commensurately to be equal to the footprint diameter. In contrast, the variances of residual noise in u_g and v_g depend on the footprint diameter through their dependencies on the variance σ_h^2 of unsmoothed SSH noise that itself depends on the footprint diameter. The factor-of-4 difference between the values of σ_h^2 for footprint diameters of 1 and 2 km on the right sides of (3b) and (4b) exists for any choice of filter cutoff wavelength λ_c. With increased smoothing, however, this factor-of-4 difference is moderated by the lagged autocorrelations inside the square brackets that increase with increasing λ_c. Because the lag distances $2\Delta x$ and $2\Delta y$ are twice as large for the commensurate grid spacings associated with the 2-km footprint diameter as for the 1-km footprint diameter, the autocorrelation values at these lags are always smaller for the larger footprint diameter. For small half-power filter cutoff wavelength λ_c, these differences in the lagged autocorrelation values are substantial.

Although not readily apparent, the terms in square brackets in (3) and (4) converge with increasing λ_c toward values that are a factor of 4 larger for the 2-km footprint diameter than for the 1-km footprint diameter. This factor-of-4 increase offsets the factor-of-4 smaller value of σ_h^2 for the 2-km footprint diameter. The net effect is that the variances of the residual noise in smoothed estimates of u_g and v_g from the two footprint diameters converge with increasing λ_c. An intuitive explanation for the convergence of the variances of the residual noise in u_g and v_g for the two footprint diameters with increasing λ_c is given later in section 4 from the equations for the wavenumber spectra of smoothed u_g and v_g noise.

The dependencies of the standard deviations $\overline{\sigma}_{u_g}$ and $\overline{\sigma}_{v_g}$ of the residual noise in smoothed estimates of u_g and v_g on filter cutoff wavelength λ_c obtained from (3) and (4) are shown as functions of λ_c in Fig. 1b for SWOT data with footprint diameters of 1 and 2 km (the thin and thick lines, respectively). As in appendix D, we used the value of $f_{37°N} = 8.75 \times 10^{-5}$ s^{-1} for the Coriolis parameter at 37°N in (3) and (4). This corresponds to the central latitude of the domain of the model of the California Current System used in this study (see Fig. 3). The values of $\overline{\sigma}_{u_g}$ and $\overline{\sigma}_{v_g}$ for a given footprint diameter are indistinguishable from each other. The above-noted rapid convergence of the standard deviations of the residual noise in smoothed estimates of u_g and v_g with increasing λ_c for the two footprint diameters is evident from Fig. 1b. The two curves become barely distinguishable for $\lambda_c \gtrsim 20$ km. The dependence on λ_c at filter cutoff wavelengths longer than 20 km

can be very closely approximated by a power-law dependence on λ_c,

$$\overline{\sigma}_{u_g} = \overline{\sigma}_{v_g} \approx \hat{a}_{u,v}\lambda_c^{-2}, \tag{5}$$

where $\hat{a}_{u,v} = 31.64 \text{ m s}^{-1} \text{ km}^2$ is the empirically determined (signified by the hat) least squares estimate of the scaling parameter. For latitudes other than 37°N, this value of $\hat{a}_{u,v}$ must be multiplied by $f_{37°N}/f$, where f is the Coriolis parameter at the latitude of interest.

For the analysis presented here, vorticity was estimated from three-point centered differences of geostrophically computed velocity components at adjacent grid points, which were themselves estimated from three-point centered differences of SSH at adjacent grid points (see the discussion in the footnote in appendix D). For a uniform grid spacing $\Delta y = \Delta x$ equal to the footprint diameter, the variance of the residual noise in geostrophically computed vorticity after isotropic two-dimensional smoothing can be expressed in terms of the variance $\overline{\sigma}_h^2$ of the smoothed SSH measurement noise by Eq. (G.21) of C19, which is

$$\overline{\sigma}_{\zeta_g}^2 = \frac{g^2}{f^2}\frac{1}{(4\Delta x^2)^2}\big[20 + 4\overline{\rho}_h(4\Delta x) - 32\overline{\rho}_h(2\Delta x) \\ + 8\overline{\rho}_h(2\sqrt{2}\Delta x)\big]\overline{\sigma}_h^2. \tag{6a}$$

This is the same as the expression (D7) for the variance of noise in unsmoothed ζ_g, except with overbars to indicate the variances and lagged correlations of smoothed estimates. The lagged autocorrelations for smoothed SSH inside the square brackets of (6a) are always larger than their counterpart lagged autocorrelations for unsmoothed SSH inside the square brackets in (D7). For this case of $\Delta y = \Delta x$, substitution of (1) for $\overline{\sigma}_h^2$ expresses $\overline{\sigma}_{\zeta_g}^2$ in terms of the variance σ_h^2 of unsmoothed SSH noise,

$$\overline{\sigma}_{\zeta_g}^2 = \frac{g^2}{f^2}\frac{1}{4\lambda_c^2\Delta x^2}\big[20 + 4\overline{\rho}_h(4\Delta x) - 32\overline{\rho}_h(2\Delta x) \\ + 8\overline{\rho}_h(2\sqrt{2}\Delta x)\big]\sigma_h^2. \tag{6b}$$

As in the cases of the variances (3) and (4) of the residual noise in smoothed estimates of u_g and v_g, the variance $\overline{\sigma}_{\zeta_g}^2$ of the residual noise in smoothed ζ_g in the form (6b) can be calculated for any choice of half-power filter cutoff wavelength λ_c from the variance σ_h^2 of the unsmoothed SSH noise for the footprint diameter of interest, the specified grid spacings Δx and Δy [assumed to be the same in (6)] and the three lagged autocorrelations of smoothed SSH on the right side of (6). Whereas $\overline{\sigma}_{u_g}^2$ and $\overline{\sigma}_{v_g}^2$ depend on the autocorrelation of smoothed SSH at the single lag $2\Delta x$, the variance $\overline{\sigma}_{\zeta_g}^2$ of the residual noise in smoothed estimates of ζ_g depends on the autocorrelations of smoothed SSH at lags of $2\Delta x$, $2\sqrt{2}\Delta x$ and $4\Delta x$.

The standard deviation of the residual noise in smoothed estimates of ζ_g obtained from (6) and normalized by the Coriolis parameter f are shown as a function of filter cutoff wavelength λ_c in Fig. 1c. We again used the value of $f_{37°N}$ for the Coriolis parameter. The differences between the standard

deviations of the smoothed ζ_g noise for the footprint diameters of 1 and 2 km (the thin and thick lines, respectively) are substantial for small λ_c but converge rapidly with increasing λ_c, becoming barely distinguishable for $\lambda_c \gtrsim 30$ km. At wavelengths longer than 30 km, the standard deviation of the vorticity noise normalized by the Coriolis parameter $f_{37°N}$ can be very closely approximated by a power-law dependence on λ_c,

$$\frac{\overline{\sigma}_{\zeta_g}}{f_{37°N}} \approx \hat{a}_\zeta\lambda_c^{-3}, \tag{7}$$

where $\hat{a}_\zeta = 5222 \text{ km}^3$ is the empirically determined least squares estimate of the scaling parameter. For latitudes other than 37°N, this value of $\hat{a}_\zeta$ must be multiplied by $(f_{37°N}/f)^2$. The squared dependence on the ratio $f_{37°N}/f$ arises from the combination of the Coriolis parameter in the denominator of (7) and the inverse dependence of $\overline{\sigma}_{\zeta_g}$ on the Coriolis parameter in the square root of (6).

Numerical values of the standard deviations $\overline{\sigma}_h$, $\overline{\sigma}_{u_g}$, $\overline{\sigma}_{v_g}$, $\overline{\sigma}_{\zeta_g}$, and $\overline{\sigma}_{\zeta_g}/f$ of the residual noise in the smoothed variables are listed in the bottom half of Table 1 for four choices of the half-power filter cutoff wavelength λ_c. The case of $\lambda_c = 15$ km corresponds to the filtering in the specification of the science requirements for SWOT estimates of SSH that are discussed in appendix A. The cases of $\lambda_c = 30$, 50, and 70 km that are listed in the table include all of the choices of smoothing that are applied for the spectra in section 4 and for the maps in section 5.

The variances $\overline{\sigma}_h^2$, $\overline{\sigma}_{u_g}^2$, $\overline{\sigma}_{v_g}^2$, and $\overline{\sigma}_{\zeta_g}^2$ of the residual noise of the smoothed variables computed from (1), (3), (4), and (6) could have been computed alternatively from Parseval's theorem (C2) in appendix C by integrating the wavenumber spectra of the residual noise after smoothing, as presented below in section 4. An advantage of that approach is that the expressions for the spectra isolate the separate filtering operations from the smoothing and the three-point centered differencing on the residual variances of the smoothed noise computed from SWOT data. For grid spacings Δx and Δy equal to the footprint diameter that is the minimum interval at which the SSH noise is uncorrelated, the products $\Delta x\Delta y\,\sigma_h^2$ that appear in the equations for the spectra of all of the smoothed variables (see section 4) are independent of footprint diameter, as discussed previously from (1). The only differences between the expressions for the footprint diameters of 1 and 2 km are thus the factors that involve the response function (E2) of the three-point centered difference estimates of the derivatives. The differences between the thin and thick lines in Figs. 1b and 1c are thus solely attributable to the filtering effects of finite-difference approximations of the derivatives on the different grids. This point is discussed further in section 4.

4. The wavenumber spectra of smoothed noise in SWOT estimates of SSH, velocity, and vorticity

The equations for the swath-averaged along-track wavenumber spectra of noise in SWOT estimates of SSH, u_g, v_g, and ζ_g after isotropic two-dimensional smoothing in postprocessing are derived in appendix I.2 of C19. As in section 3, we

consider only the cases of footprint diameters of 1 and 2 km since the noise is so large for a footprint diameter of 0.5 km. The spectrum of smoothed SSH noise is derived straightforwardly to obtain Eq. (I.27) of C19, which is

$$\overline{S}_h(l) = 4\Delta x \Delta y\, \sigma_h^2\, W_{\lambda_c}^2(l) \int_0^{k_N} W_{\lambda_c}^2(k)\, dk \qquad (8a)$$

$$= 2\Delta x\, S_h(l)\, W_{\lambda_c}^2(l) \int_0^{k_N} W_{\lambda_c}^2(k)\, dk, \qquad (8b)$$

where $W_{\lambda_c}(k)$ and $W_{\lambda_c}(l)$ are the filter transfer functions of the smoother applied in the orthogonal across-track x and along-track y dimensions with a half-power filter cutoff wavelength of λ_c in each dimension. The form (8b) follows from Parseval's theorem (C3) that relates the integral of the constant white-noise spectrum $S_h(l)$ to the variance of the uncorrelated SSH errors.

The expressions (8a) and (8b) are based on separate one-dimensional smoothing in the orthogonal x and y dimensions, which are defined here to be across track and along track, respectively. For the Parzen smoother used in this study, this is essentially equivalent to isotropic two-dimensional smoothing with a Gaussian smoother, as discussed previously at the beginning of section 3. This is approximately true for most other choices of smoothing. The advantage of separate smoothing in two orthogonal dimensions is that it allows the simple analytical forms (8a) and (8b) for the spectrum of smoothed SSH noise and analogously simple analytical expressions for the spectra of smoothed u_g, v_g, and ζ_g that are presented below. It can be seen from (8b) that smoothing in the across-track dimension attenuates the along-track spectrum $S_h(l)$ of unsmoothed noise for the specified footprint diameter (see appendix C) by the constant multiplicative factor

$$c_{\lambda_c} = 2\Delta x \int_0^{k_N} W_{\lambda_c}^2(k)\, dk \qquad (9)$$

at all wavenumbers l. Note that $2\Delta x = k_N^{-1}$, which is the Nyquist wavenumber associated with the sample interval Δx. In addition to this uniform attenuation at all wavenumbers, it can be seen from (8b) that $S_h(l)$ is attenuated at high wavenumbers l by the along-track filter transfer function $W_{\lambda_c}^2(l)$. The details of this wavenumber-dependent attenuation depend on the filter transfer function $W_{\lambda_c}(l)$ of the particular smoother applied to the unsmoothed SWOT estimates of SSH.

For the Parzen smoother used in C19 and in this study, it is shown in appendix A of C19 that the filter transfer function in the across-track dimension x is

$$W_{\lambda_c}(k) = \left[\frac{\sin(\pi k \lambda_c/4)}{\pi k \lambda_c/4} \right]^4. \qquad (10)$$

The filter transfer function $W_{\lambda_c}(l)$ in the along-track dimension y is the same, except with across-track wavenumber k replaced with along-track wavenumber l. From Eq. (I.28) of C19, the integral of the square of the filter transfer function

$W_{\lambda_c}(k)$ that appears in (8) and (9) has a simple approximate form in the case of the Parzen smoother,

$$\int_0^{k_N} W_{\lambda_c}^2(k)\, dk \approx \frac{1}{\lambda_c}. \qquad (11)$$

The attenuation factor (9) for the Parzen smoother is therefore

$$c_{\lambda_c} \approx \frac{2\Delta x}{\lambda_c}. \qquad (12)$$

The value of the integral (11), and thus the attenuation factor (9), are very similar for other smoothers when the parameters of the smoother are calibrated to give the same half-power filter cutoff wavelength λ_c.

The solution (12) for c_{λ_c} can be understood qualitatively from consideration of smoothing with a simple running average. In one dimension with a span of $M\Delta x$ for a grid spacing Δx on which the measurement noise is uncorrelated, i.e., a grid spacing equal to or larger than the footprint diameter (see appendix B.1 of C19), a block average of M uncorrelated observations reduces the noise variance by the well-known factor of M^{-1}. It is shown in appendix A of C19 that the half-power filter cutoff wavelength for running averages with a span of $M\Delta x$ is given approximately by $\lambda_c = 2M\Delta x$. The number of points in the block average is thus related to the filter cutoff wavelength by $M = \lambda_c/(2\Delta x)$. The noise variance reduction factor can therefore be expressed in terms of the filter cutoff wavelength as $M^{-1} = 2\Delta x \lambda_c^{-1}$. This is equivalent to the attenuation factor (12).

The wavenumber spectrum of residual noise in estimates of u_g after isotropic two-dimensional smoothing in postprocessing is given by the unnumbered equation before Eq. (I.31a) of C19,

$$\overline{S}_{u_g}(l) = \frac{g^2}{f^2} 4\Delta x \Delta y\, \sigma_h^2 \left| W_{3\text{pt}}(l, \Delta y) \right|^2 W_{\lambda_c}^2(l) \int_0^{k_N} W_{\lambda_c}^2(k)\, dk, \qquad (13)$$

where $W_{3\text{pt}}(l, \Delta y)$ is the response function (E2) for along-track three-point centered differences. Equation (13) is similar to its counterpart relation (E1a) between the spectrum $S_{u_g}(l)$ of unsmoothed u_g noise and the SSH noise standard deviation σ_h^2, except with the added effects of smoothing in each dimension appearing on the right side of (13).

The wavenumber spectrum of residual noise in estimates of v_g after isotropic two-dimensional smoothing in postprocessing is Eq. (I.33a) of C19, which is

$$\overline{S}_{v_g}(l) = \frac{g^2}{f^2} 4\Delta x \Delta y\, \sigma_h^2\, W_{\lambda_c}^2(l) \int_0^{k_N} W_{\lambda_c}^2(k) \left| W_{3\text{pt}}(k, \Delta x) \right|^2 dk, \qquad (14)$$

where $W_{3\text{pt}}(k, \Delta x)$ is the response function for across-track three-point centered differences analogous to (E2) but with across-track wavenumber k and grid spacing Δx rather than along-track wavenumber l and grid spacing Δy. Equation (14) is similar to its counterpart relation (E3a) between the spectrum $S_{v_g}(l)$ of unsmoothed v_g noise and the SSH noise standard

deviation σ_h^2, except again with the added effects of smoothing in each dimension appearing on the right side of (14).

The expressions (13) and (14) for the spectra of u_g and v_g noise after smoothing in postprocessing provide mathematical explanations for the convergence with increasing filter cutoff wavelength λ_c of the variances of the residual noise in u_g and v_g for the footprint diameters of 1 and 2 km that was noted in section 3 from Fig. 1b. This can be understood intuitively by noting that the spectra (13) and (14) of smoothed estimates of u_g and v_g noise involve products of the response function for three-point centered differences and the filter transfer function of the smoothing with a half-power filter cutoff wavelength of λ_c. The latter depends only on λ_c and not on the footprint diameter [see Eq. (10) for the case of the Parzen smoother used in this study], but the response function for three-point centered differences differs for the different grid spacings associated with the two footprint diameters. In particular, the bandpass filtering property of the $\sin^2$ dependence on the square of the response function (E2) attenuates more of the high-wavenumber variability for the footprint diameter and grid spacing of 2 km compared with the footprint diameter and grid spacing of 1 km. This dependence on grid spacing is shown in Fig. H.1 of C19 in the context of finite differences on sample grids with grid spacings of 1 and 5 km.

For any particular choice of footprint diameter and grid spacing, the bandpass filtering from the response function for three-point centered differences is the same for any choice of spatial smoothing. As the half-power filter cutoff wavelength λ_c of the smoothing is increased, the filter transfer function of the smoothing attenuates progressively more of the variability at lower wavenumbers. This low-pass filtering eventually attenuates the variance within the wavenumber band over which the response functions for three-point centered differences differ on the sample grid spacings of 1 and 2 km for the respective footprint diameters of 1 and 2 km. The effects of this double filtering can be seen from Fig. H.2 of C19 in the context of finite differencing on sample grids with spacings of 1 and 5 km. The convergence of the standard deviations of the residual noise in Fig. 1b for the footprint diameters of 1 and 2 km thus occurs because the differences between the response functions for three-point centered differences on the two grid spacings become progressively more attenuated with increased spatial smoothing.

The wavenumber spectrum of residual noise in estimates of ζ_g after isotropic two-dimensional smoothing is Eq. (I.35b) of C19, which can be written as

$$\overline{S}_{\zeta_g}(l) = \frac{g^2}{f^2} 4\Delta x \Delta y \, \sigma_h^2 \, W_{\lambda_c}^2(l) \left[\int_0^{k_N} W_{\lambda_c}^2(k) \left| W_{3pt}(k, \Delta x) \right|^4 dk \right.$$
$$+ 2 \left| W_{3pt}(l, \Delta y) \right|^2 \int_0^{k_N} W_{\lambda_c}^2(k) \left| W_{3pt}(k, \Delta x) \right|^2 dk$$
$$\left. + \frac{1}{\lambda_c} \left| W_{3pt}(l, \Delta y) \right|^4 \right]. \tag{15}$$

This expression is much more complicated than its counterpart relation (E4) for the spectrum $S_{\zeta_g}(l)$ of unsmoothed noise

in ζ_g. This is because the smoothing and the three-point centered differencing affect both terms in the expression (D2) for ζ_g and both of these filtering operations are applied in both dimensions.

It can be noted that the first two terms in the spectrum (15) of smoothed estimates of ζ_g involve the product of the response function $W_{3pt}(k, \Delta x)$ for three-point centered differences and the filter transfer function $W_{\lambda_c}(k)$ of the smoothing with a half-power filter cutoff wavelength of λ_c. As discussed above from (13) and (14), the differences between these products for the footprint diameters of 1 and 2 km decrease with increased filter cutoff wavelength λ_c. This explains the convergence of the standard deviations of the residual noise in Fig. 1c for the footprint diameters of 1 and 2 km.

The expressions (8), (13), (14), and (15) are applicable to any low-pass filter with half-power filter cutoff wavelength λ_c, with the caveat that the equivalence of isotropic two-dimensional smoothing and separate one-dimensional smoothing in two orthogonal dimensions is less valid for some choices of smoothing operation than for the Parzen smoother used in this study.

The spectra of noise in SSH, u_g, v_g, and ζ_g computed from (8), (13), (14), and (15), respectively, are shown in Fig. 2 after applying isotropic two-dimensional Parzen smoothing in postprocessing of simulated SWOT estimates of SSH for footprint diameters of 1 and 2 km (thin and thick red lines, respectively) and half-power filter cutoff wavelengths of 15, 30, and 50 km. For reference, the noise spectra from Fig. E1 of unsmoothed variables for the footprint diameter of 2 km that will likely be the SWOT product preferred by most users are shown by the purple dashed lines in each panel. As discussed in appendix A, the choice of $\lambda_c = 15$ km in Fig. 2 corresponds to the filtering applied in the specification of the science requirements for SWOT estimates of SSH. The other two choices of λ_c in this figure illustrate the decrease with increasing λ_c of the spectral power of the noise at all wavenumbers in the SWOT estimates of each variable. The rapid convergence of the noise spectra of smoothed u_g, v_g, and ζ_g for the two footprint diameters is also apparent, as was discussed above from (13), (14), and (15) and in section 3 from the standard deviations of the smoothed noise in Figs. 1b and 1c. Differences between the spectra of smoothed u_g and v_g noise for the two footprint diameters can be seen for $\lambda_c = 15$ km but the two noise spectra are indistinguishable for the cases of $\lambda_c = 30$ and 50 km. The spectra of smoothed ζ_g noise for the two footprint diameters are barely distinguishable for $\lambda_c = 30$ km but become indistinguishable for the case of $\lambda_c = 50$ km.

The distinctions between the wavenumber dependencies of the smoothed noise and the smoothed signals of SSH, u_g, v_g and ζ_g from the model of the California Current System considered in this study (see section 5) can be seen from comparison of the spectra shown by the red and thick black lines, respectively. For reference, the thin black lines are the spectra of the unsmoothed signals. The two-dimensional smoothing attenuates both the signal and the noise spectra at wavenumbers higher than the filter cutoff wavelength of λ_c^{-1}. The noise spectra for

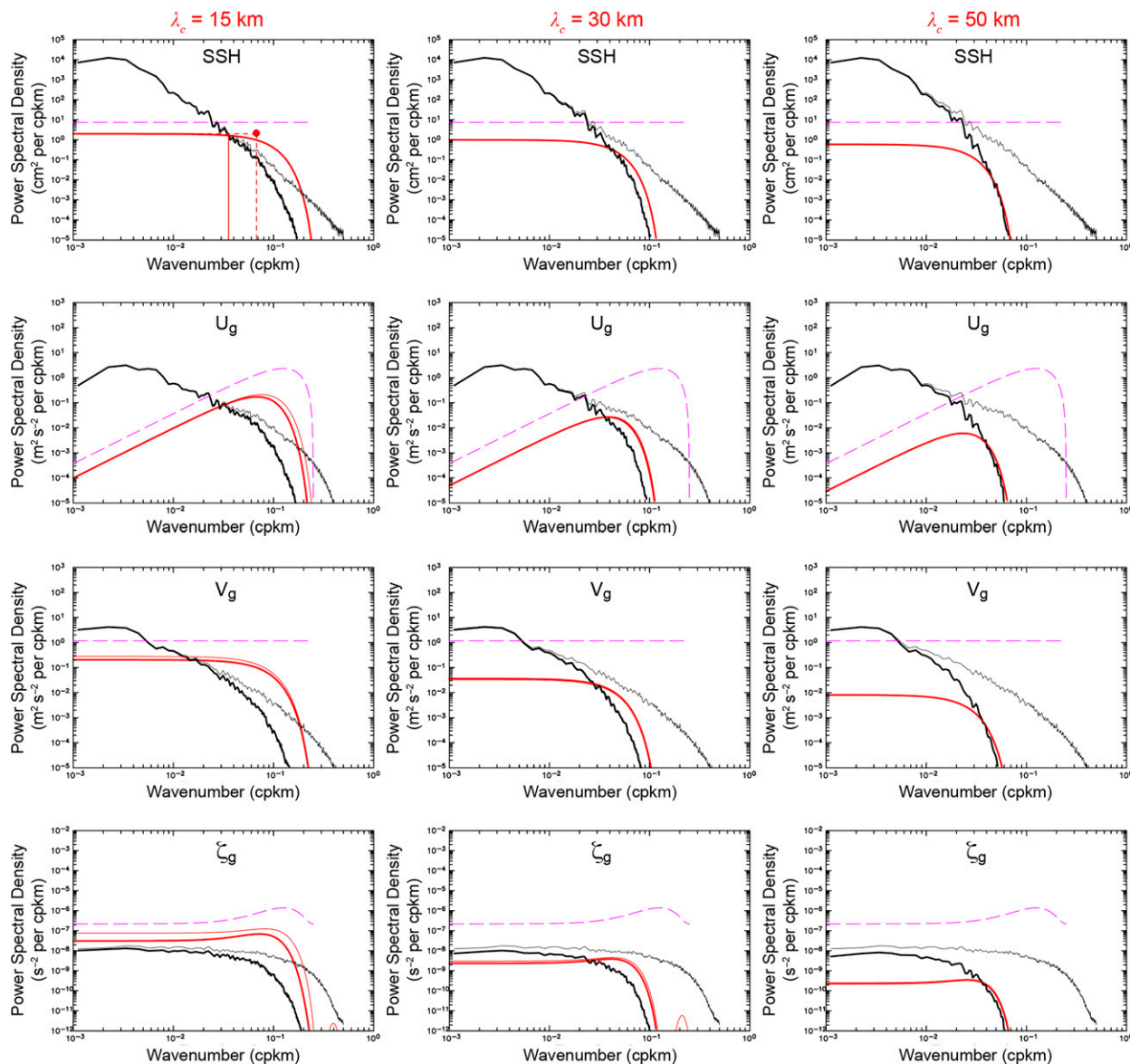# Wavenumber Spectra for Filter Cutoffs of 15 km, 30 km and 50 km

FIG. 2. Swath-averaged wavenumber spectra of smoothed signals (thick black lines) computed in the alongshore dimension of the model of the California Current System (CCS) considered here (see section 5) for which descending swaths of SWOT are approximately parallel to the coast (see Fig. 3) and smoothed noise (red lines) in SWOT estimates of SSH, velocity components u_g and v_g computed geostrophically from SSH based on the Coriolis parameter $f_{37°N} = 8.75 \times 10^{-5}$ s^{-1} at the central latitude 37°N of the CCS model, and vorticity ζ_g computed from u_g and v_g. The spectra of residual errors after smoothing the SWOT noise using a Parzen smoother with half-power filter cutoff wavelengths of (left to right) $\lambda_c = 15$, 30, and 50 km are shown for footprint diameters of 1 and 2 km (thin and thick red lines, respectively, which become less distinguishable with increasing λ_c). The horizontal and vertical red dashed and solid lines and the red dot in the top-left panel are as in Fig. E1. For reference, the purple dashed lines are the spectra of unsmoothed noise for the footprint diameter of 2 km and the thin black lines are the spectra of unsmoothed signals (see Fig. E1).

all of the variables are further attenuated progressively more at lower wavenumbers with increasing λ_c. The ζ_g spectrum is also somewhat attenuated at lower wavenumbers with increasing λ_c, but much less so than the ζ_g noise spectrum. In all cases, the noise spectra are attenuated much more quickly than the

signal spectra with increasing λ_c, thus improving the signal-to-noise ratio. For all four variables, smoothing with a half-power filter cutoff wavelength of at least $\lambda_c = 50$ km is required for the residual noise spectra to become less energetic than the smoothed signal spectra at all wavenumbers.

5. Example maps of simulated noisy SWOT estimates of SSH, velocity, and vorticity

A visual assessment of the effects of the statistical characterizations of the noise in sections 2–4 on SWOT estimates of SSH and geostrophically computed velocity and vorticity is presented in this section from maps constructed from simulated SWOT data based on the Regional Oceanic Modeling System (ROMS) model of the California Current System (CCS) that was considered by C19. The details of this model are summarized by Molemaker et al. (2015) and in section 2 of C19. The model does not include tides, was forced only by seasonal winds, has a high dissipation that attenuates internal wave variability, and has vertical and horizontal grid resolutions that are not adequate to resolve the full spectrum of internal wave variability. The small-scale features of tides and internal waves are therefore likely underestimated in the model used in this study. The conclusions from the analysis presented here may thus be an overly optimistic assessment of the capabilities for SWOT estimates of velocity and vorticity.

An instantaneous snapshot of SSH for the full model domain on the 0.5 km × 0.5 km grid of the model is shown in Fig. 3a. The speed of the associated geostrophically computed velocity based on the local Coriolis parameter at each grid location is shown in Fig. 3b and the geostrophically computed vorticity normalized by the local Coriolis parameter is shown in Fig. 3c. A descending pair of the parallel swaths from a single simulated overpass of SWOT is overlaid on each of these three maps. This simulated SWOT overpass samples the meandering core of the southward California Current. For reference, the full set of measurement swaths during each 21-day repeat of the SWOT orbit within the bounds of the map is shown in Fig. 3d. The different colors illustrate the 10-day subcycle of the SWOT orbit that is discussed in section 6; the swaths shown in red will be sampled about 10 days earlier and 10 days later than the swaths shown in blue.

To the untrained eye, the submesoscale features that the SWOT mission seeks to observe are difficult to identify in the error-free SSH field in Fig. 3a because the variance of SSH is so small on scales smaller than 50 km. They are evident as subtle yellow dimples imbedded in the orange, light red and green areas of the larger mesoscale features in the SSH field. The spatial high-pass filtering from differentiation of the SSH field emphasizes these submesoscale features in the geostrophically computed speed field shown in Fig. 3b. The submesoscale features are even more emphasized in the geostrophically computed vorticity field in Fig. 3c that was calculated from double differentiation of the SSH field. For the analysis in this study, the simulated SSH fields at the model grid points within the simulated SWOT measurement swaths were used directly without consideration of the differences in location and orientation of the model grid relative to the swath-based grids of the SSH estimates that will be provided by the SWOT Project.

To simulate SWOT data, the SSH field in Fig. 3a was smoothed isotropically with the half-power filter cutoff wavelength of 4 km that is the minimum filter cutoff for a footprint diameter of 2 km. (As discussed in appendixes B and C, the SWOT Project may smooth the SSH with a half-power filter cutoff wavelength somewhat longer than 4 km for the 2 km × 2 km data product.) The smoothed SSH field on the 0.5 km × 0.5 km grid of the model was then subsampled on a 2 km × 2 km grid within the two parallel swaths of the simulated SWOT overpass, thus mimicking the SWOT data product that will likely be preferred by most users. As in the previous sections, this simulated SWOT data product is referred to here as "unsmoothed" to distinguish it from the SSH field obtained by additional smoothing in the simulated postprocessing considered below. Spatially homogeneous uncorrelated SSH measurement errors with the swath-averaged standard deviation of σ_{2km} = 1.37 cm that is derived in appendix C for a footprint diameter of 2 km with 4-km smoothing were added to the gridded values of the model SSH field. The across-swath variations of the measurement noise shown in Fig. C1 and the long-wavelength measurement errors discussed in appendix A are not considered here. Simulated SWOT estimates of velocity and vorticity were computed geostrophically from the error-free and noisy SSH fields with the derivatives approximated as three-point centered differences.

To see the improvement of the signal-to-noise ratio in maps of smoothed SSH, velocity, and vorticity constructed from noisy simulated SWOT measurements of SSH, the unsmoothed error-free and noisy SSH fields within only the measurement swaths were smoothed two-dimensionally in simulated postprocessing using the Parzen smoother with selected choices of half-power filter cutoff wavelength. The residual effects of measurement noise on the smoothed SWOT estimates of SSH, velocity, and vorticity are assessed here from consideration of the subregion near the coast in the center of the CCS model domain that is indicated by the small rotated box in each panel of Fig. 3. For reference, the California calibration and validation site for SWOT is centered at 35.7°N, 125.4°W, which is near the bottom-left corner of the small rotated boxes. The SSH and geostrophically computed speed and vorticity within the small box are shown in the left column of Fig. 4 in rotated coordinates that are aligned with the model grid. These three error-free maps are the same as in the subdomain of the full-resolution maps in Fig. 3, except they have been smoothed and subsampled as summarized above to simulate the SWOT data product with a footprint diameter of 2 km. The edges of the pair of swaths in the simulated single descending overpass of SWOT that are shown in Figs. 3a–c are indicated by the parallel lines overlaid on each panel in the left column of Fig. 4.

The other four columns in Fig. 4 show the error-free and noisy fields (the left and right pair of swaths in each column) sampled only within the pair of measurement swaths from the simulated SWOT overpass. These four columns correspond to the fields constructed from the simulated SWOT data with smoothing applied based only on SSH observations within the measurement swaths with half-power filter cutoff wavelengths of λ_c = 0 km (i.e., no smoothing), 15, 30, and 50 km. The filter cutoff of 15 km corresponds to the smoothing in the specification of the science requirements for SWOT (see appendix A). According to the criteria proposed in section 5 of C19, the
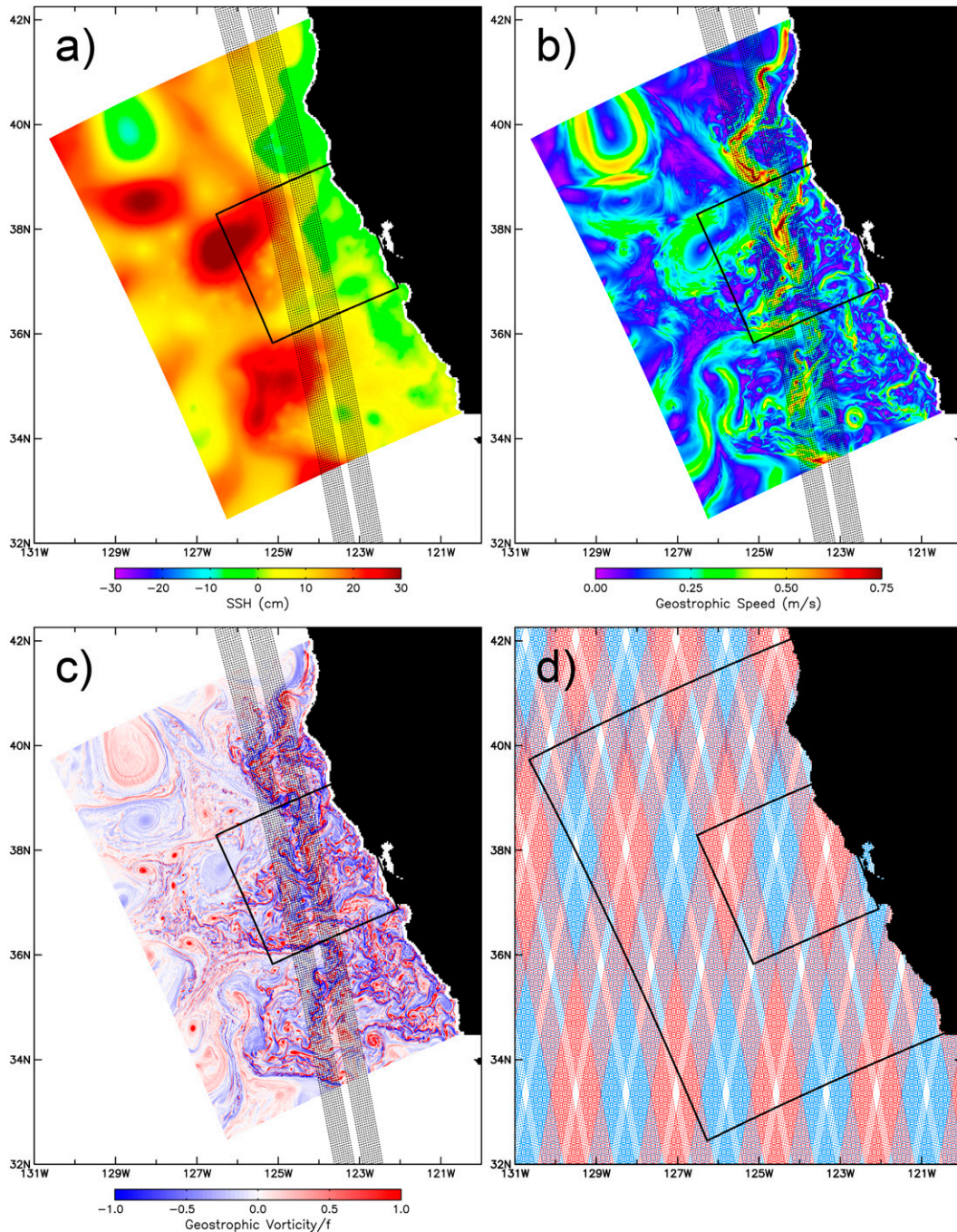
FIG. 3. Maps of error-free instantaneous (a) SSH, (b) the magnitude of geostrophically computed velocity, and (c) the geostrophically computed vorticity for model day 27 May on the 0.5 km × 0.5 km grid of the model of the CCS considered here. (d) Simulated SWOT measurement swaths during two 5-day periods that are separated by 10 days in the 21-day exact repeat SWOT orbit (blue for days 3–8 and red for days 13–18). The diamond-shaped holes in the sampling pattern in (d) are never observed during the 21-day SWOT orbit. The shaded regions in (a)–(c) are the pair of simulated SWOT measurement swaths for the single descending overpass over the CCS model domain that is considered in Figs. 4 and 5. The large box in (d) is the full CCS model domain and the small box in each panel is the subregion of the CCS model that is shown in rotated coordinates in Figs. 4 and 5. The California calibration and validation site for SWOT is centered at 35.7°N, 125.4°W near the bottom-left corner of the small boxes.
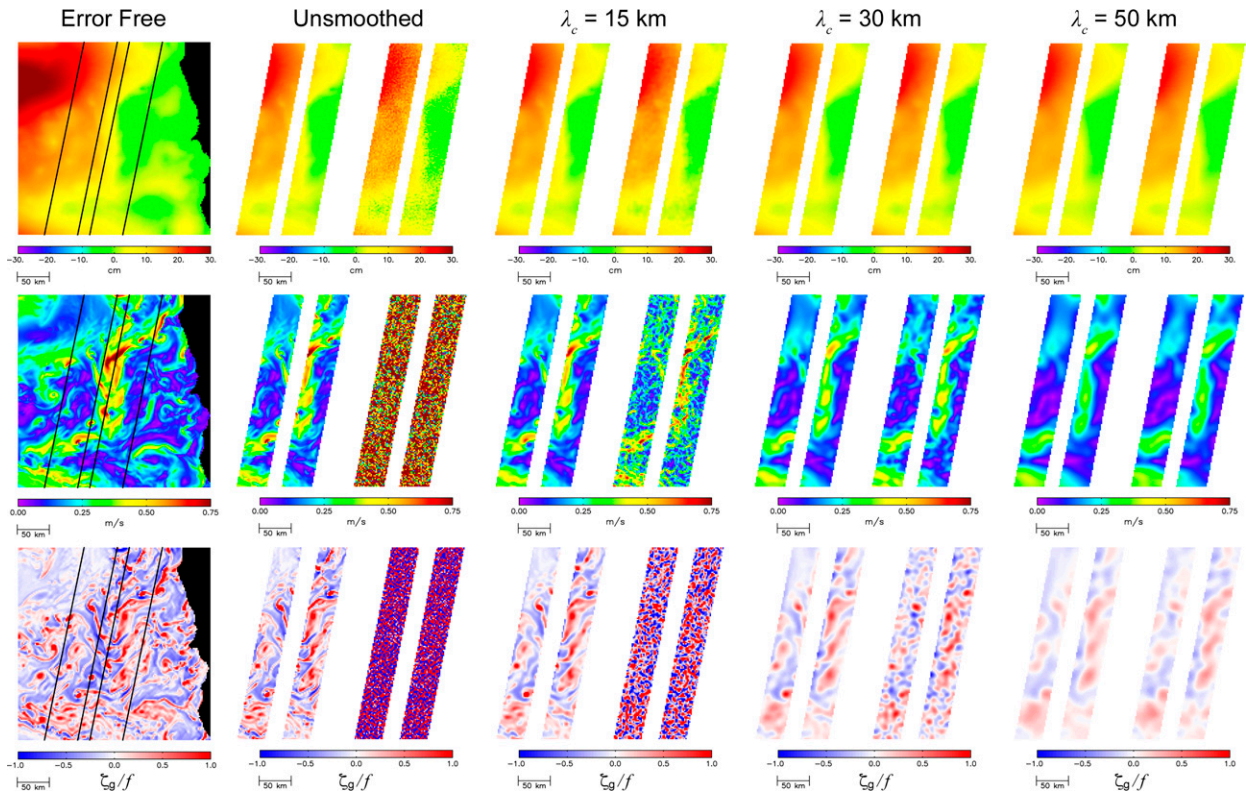
FIG. 4. (left) Example maps of instantaneous error-free (top) SSH, (middle) the magnitude of geostrophically computed velocity, and (bottom) geostrophically computed vorticity for model day 27 May within the region of the CCS model shown by the small boxes in Fig. 3. The maps have been rotated by a polar angle of 24° relative to the latitude–longitude coordinates in Fig. 3 to align with the grid of the CCS model. The geostrophic calculations are based on the local Coriolis parameter f at each grid point and the parallel lines in the left panels are the swath edges for the simulated overpass of SWOT shown in Figs. 3a–c. (right four columns, top to bottom) SSH, geostrophically computed speed, and vorticity based only on simulated data within the measurement swaths of the single overpass of SWOT for a footprint diameter of 2 km on a 2 km × 2 km grid smoothed using a Parzen smoother with half-power filter cutoff wavelengths of $\lambda_c = 0$ km (i.e., unsmoothed), 15, 30, and 50 km. The left pair of swaths in each column shows the smoothed fields without measurement errors and the right pair of swaths includes the effects of spatially homogeneous uncorrelated SSH measurement errors with the standard deviation of $\sigma_{2km} = 1.37$ cm for the footprint diameter of 2 km.

filter cutoffs of 30 and 50 km correspond approximately to the resolution capabilities of instantaneous maps of geostrophically computed velocity and vorticity, respectively (see Figs. 17b,c and 18 and the top panels of Fig. 51 of C19). Note, however, that the analysis of the resolution capability in instantaneous maps in section 6 of C19 did not take into consideration the edge-effect sampling errors that are discussed below.

Consider first the fields constructed from unsmoothed simulated SWOT data that are shown in the second column of Fig. 4. The noise in the SSH measurements is apparent from the speckles in the right pair of swaths. The effects of this visually subtle SSH measurement noise on SWOT estimates of velocity and vorticity completely swamp the submesoscale features in the unsmoothed maps of both of these derivative fields. The noise standard deviations of 0.54 m s^{-1} in each velocity component and 4.9f in the vorticity estimates (see the fourth row in the top half of Table 1) are much more energetic because of the amplifications of the effects of SSH measurement noise discussed in appendix D that arise from the

finite-difference approximations of the derivatives. It can be inferred from these maps that velocity and vorticity fields will not likely be detectable on any scales from unsmoothed SWOT data, at least in the CCS region considered here, and likely in most regions of the World Ocean. Additional smoothing in postprocessing will be required to attenuate the uncorrelated measurement errors and improve the signal-to-noise (S/N) ratio.

When the simulated SWOT data are smoothed within the measurement swaths with half-power filter cutoff wavelengths of 15, 30, and 50 km (third, fourth, and fifth columns of Fig. 4, respectively), the residual noise diminishes rapidly for all three variables, as shown previously in Fig. 1. The standard deviations of the residual noise in each variable are listed in the bottom half of Table 1. (Note that the residual effects of measurement errors in Table 1 and Fig. 4 do not include the edge-effect sampling errors discussed below that arise from smoothing within the narrow SWOT measurement swaths.) The signals are also attenuated by the smoothing, but not as rapidly as the noise from the effects of uncorrelated measurement

errors (see Fig. 2). The S/N ratio thus improves with increased smoothing.

For the case of SSH, the residual noise in SWOT estimates of SSH can still be seen with 15-km smoothing from close inspection of the top panel in the third column of Fig. 4. There is no visual evidence of residual SSH noise with filter cutoffs of 30 or 50 km.

For SWOT estimates of velocity, the residual noise is readily apparent in the swath maps with 15-km smoothing shown in the middle panel of the third column of Fig. 4. The most energetic features in the error-free geostrophically computed velocity field with 15-km smoothing in the left pair of swaths can be detected in the noisy field with 15-km smoothing in the right pair of swaths. However, there are numerous features in the 15-km smoothed noisy field that could easily be misinterpreted as signals without the foreknowledge of the details of the error-free smoothed field in the left pair of swaths. The residual velocity noise becomes relatively subtle with the 30-km smoothing in the middle panel of the fourth column of Fig. 4. For the threshold S/N standard deviation ratio of 3.16 recommended by C19 (corresponding to a variance ratio of 10), the resolution capability of SWOT estimates of velocity is 32 km. The resolution capability for a more liberal threshold S/N standard deviation ratio of 2 (a variance ratio of 4) is 24 km. Note, however, that the C19 assessments of the resolution capability of instantaneous maps of geostrophically computed velocity do not include consideration of the edge-effect sampling errors that are discussed below.

The challenge of estimating vorticity from SWOT data is very apparent from the bottom panels of Fig. 4. Because of the large amplification of the effects of SSH measurement noise (see appendix D) from finite difference approximations of the double derivatives required to compute vorticity geostrophically from SSH, the signals are still swamped by the noise with 15-km smoothing. With foreknowledge of the smoothed error-free field in the left pair of swaths in the bottom panel of the fourth column of Fig. 4, the features in the 30-km smoothed error-free geostrophically computed vorticity field can be identified in the 30-km smoothed noisy field in the right pair of swaths. But there are numerous energetic artifacts in the 30-km smoothed noisy field that could easily be misinterpreted as submesoscale features. The residual noise becomes relatively subtle with the 50-km smoothing in the bottom-right panel of Fig. 4. The resolution capability of SWOT estimates of instantaneous vorticity deduced by C19 is 54 km based a threshold S/N standard deviation ratio of 3.16 and 44 km for a threshold S/N standard deviation ratio of 2. We note again that these assessments of resolution capability by C19 do not take into consideration edge-effect sampling errors.

The edge-effect sampling errors alluded to several times above become readily apparent from the spatial structures of the errors of the simulated SWOT estimates of SSH, velocity, and vorticity, rather than the maps of the signals without and with noise that are shown in Fig. 4. This can be achieved for the snapshot fields considered here by subtracting smoothed fields computed from the spatially complete error-free fields in the left column of Fig. 4 from smoothed estimates computed from simulated error-free and noisy SWOT data within just the measurement swaths. For each choice of half-power filter cutoff, these errors can be partitioned into a contribution from sampling errors and a contribution from residual measurement noise. The former corresponds to the errors of the smoothed fields that would be incurred if the smoothing were applied to error-free fields within just the SWOT measurement swaths. For the case considered here in which estimates are constructed from a pair of measurement swaths from a single simulated overpass of SWOT, sampling errors consist only of edge effects of smoothing from incomplete data within the span of the smoother near the edges of the measurement swaths. When the SSH fields are constructed from space–time smoothing of SWOT data from multiple overpasses, sampling errors are also incurred from the discrete and irregular sampling of rapidly evolving small-scale features. This is briefly discussed in section 6 below and is addressed in detail in section 8 of C19. The present analysis considers only the instantaneous fields constructed from simulated SWOT data within the measurement swaths of a single overpass.

Maps of the sampling errors and residual measurement noise in smoothed swath estimates of instantaneous SSH, velocity, and vorticity are shown in the middle two columns of Fig. 5 for the half-power filter cutoff wavelengths of $\lambda_c = 30$ and 50 km that were considered in Fig. 4. The right column shows the maps for a larger filter cutoff of $\lambda_c = 70$ km to illustrate the increased edge effects with increased smoothing beyond what was considered in Fig. 4. Note that different color bars are used for all of the error maps in Fig. 5 compared with the color bars for the maps in the left column of Fig. 5 and the color bars for all of the maps in Fig. 4.

We focus first on the sampling errors from edge effects in the smoothing of error-free data that are shown in the left pair of swaths in each of the right three columns of Fig. 5. The smoothing in these figures was two-dimensional and isotropic and was applied based only on data within the two measurement swaths. For estimates at any location across the measurement swath, complete data exist in the along-track dimension. Along the center of the swath, the data in the across-track dimension are symmetrically distributed about the estimation locations but the data distributions become more and more asymmetric as the estimation locations approach the swath edges; complete data exist toward the center of the swath unless the half span of the smoothing exceeds the distance to the far edge of the swath. Toward the near edge of the swath, however, no data are available beyond the edge of the swath. At the extreme estimation locations along the swath edges, data are available only in the half plane toward the center of the swath.

With large enough half-power filter cutoff wavelength, the estimates in one swath can include some data from the other swath on the opposite side of the 20-km nadir gap. SSH data along the ground track are also available from the nadir altimeter. As discussed in the introduction, the very different measurement noise and footprint diameter complicate the merging of nadir altimeter data with the KaRIn estimates of SSH across the two measurement swaths. Data from the nadir altimeter are not considered in this study.
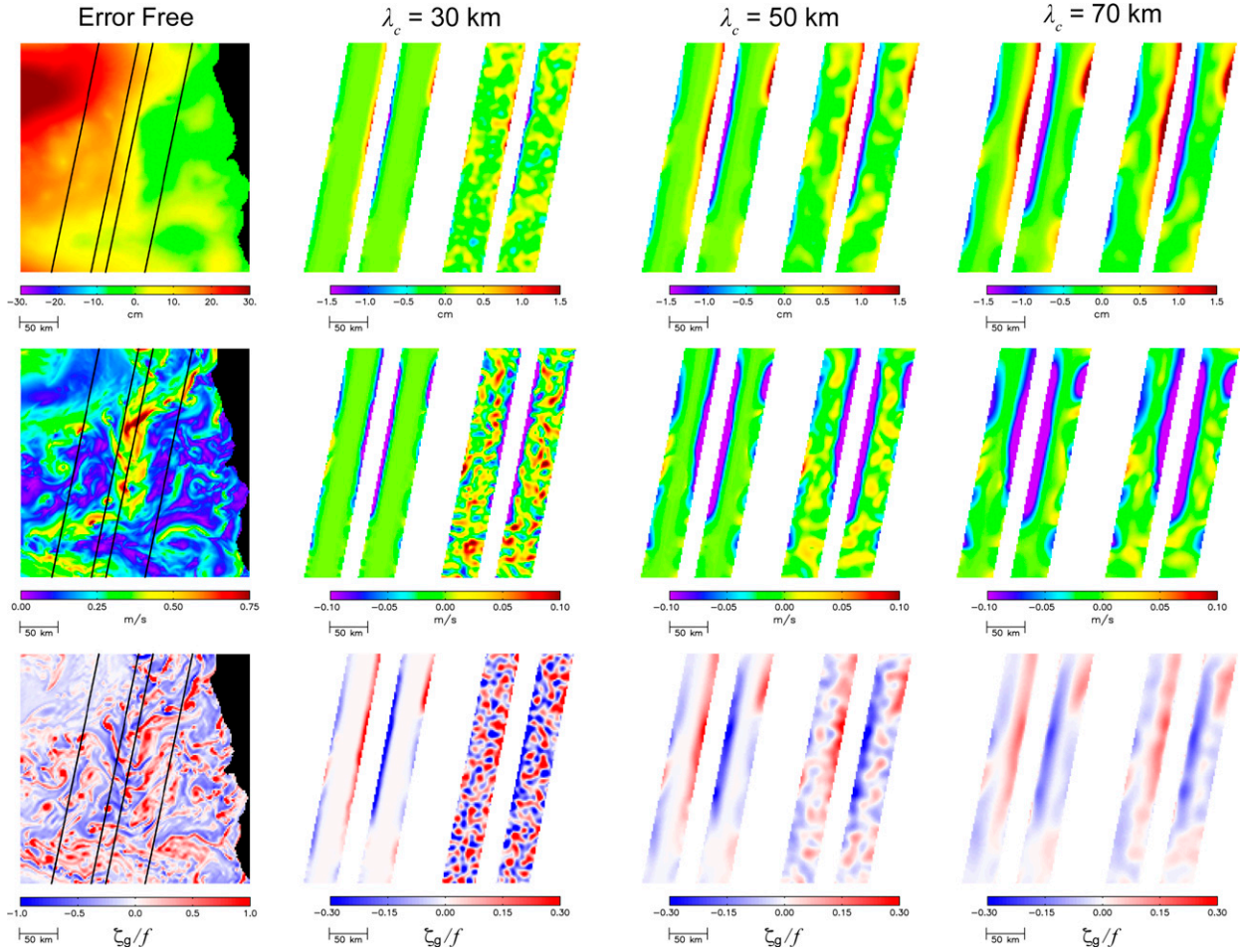
FIG. 5. (left) The same example maps in rotated coordinates as in Fig. 4 showing (top) error-free SSH, (middle) the magnitude of geo-strophically computed velocity, and (bottom) geostrophically computed vorticity. The geostrophic calculations are again based on the local Coriolis parameter *f* at each grid point and the parallel lines indicate the swath edges for the simulated overpass of SWOT shown in Figs. 3a–c. (right three columns, top to bottom) The errors of SSH, geostrophically computed speed, and geostrophically computed vortic-ity based only on simulated data within the single overpass of SWOT for a footprint diameter of 2 km on a 2 km × 2 km grid smoothed us-ing a Parzen smoother with half-power filter cutoff wavelengths of λ_c = 30, 50, and 70 km. The left pairs of swaths in each column show the edge-effect sampling errors from mapping of error-free fields and the right pairs of swaths include the effects of spatially homogeneous uncorrelated SSH measurement errors with the standard deviation of σ_{2km} = 1.37 cm for the footprint diameter of 2 km.

Edge effects are visually apparent for all three variables and all three choices of filter cutoff λ_c in the maps in the left pair of swaths in each column of Fig. 5 that were constructed by smoothing error-free simulated data within just the two parallel measurement swaths. With increased smoothing, these edge effects increase in magnitude and extend farther toward the centers of the swaths. For the case of smoothing with a half-power filter cutoff wavelength of λ_c = 70 km, all but a narrow strip along the center of each swath is contami-nated by edge effects.

For the case of a filter cutoff wavelength of λ_c = 50 km, edge-effect contamination is relatively small within approxi-mately the center half of each swath. This is perhaps surpris-ing since the width of each swath is only 50 km. This can be understood from consideration of the spatial structure of the weighting function of the two-dimensional Parzen smoother.

As discussed in section 3, the filtering properties of the Parzen smoother for a given span are very similar to those of the Gaussian smoother with an *e*-folding scale calibrated to give the same half-power filter cutoff wavelength λ_c as the Parzen smoother (see Fig. C2 in appendix C of C19). The fraction of the Parzen weighting within a given distance of each estima-tion location can therefore be closely approximated by the fraction of the Gaussian weighting within that distance. An advantage of the latter is that an analytical expression can be derived for the volume of a two-dimensional Gaussian weighting function within any radial distance from the esti-mation location. For a two-dimensional Gaussian function with an *e*-folding scale of *L*, the volume within a radius r_i is

$$V_i = \frac{1}{\pi L^2} \int_0^{2\pi} \int_0^{r_i} e^{-(r/L)^2} r \, dr \, d\theta = 1 - e^{-(r_i/L)^2}. \qquad (16)$$

Inclusion of the normalization factor $(\pi L^2)^{-1}$ yields a total volume of $V = 1$ when $r_i = \infty$, thus assuring that the weighted average is unbiased. The ratio of the volumes within any two radial distances of r_1 and r_2 from the center of the Gaussian is

$$\frac{V_1}{V_2} = \frac{1 - e^{-(r_1/L)^2}}{1 - e^{-(r_2/L)^2}}. \tag{17}$$

The e-folding scale for a Gaussian smoother that has the same half-power filter cutoff wavelength λ_c as the Parzen smoother is $L = 0.187\lambda_c$ (see appendix C of C19). The weightings for the Parzen smoother are zero for radial distances larger than a half span that is related to the filter cutoff wavelength by $r_{\max} = 0.455\lambda_c$ (see appendix A of C19). We therefore set $r_2 = r_{\max}$, which corresponds to a volume V_2 that is

$$V_{\max} = 1 - e^{-(r_{\max}/L)^2} = 1 - e^{-(0.455/0.187)^2} = 0.9973.$$

The Gaussian approximation of the fractional volume of the Parzen smoother within any specified radius $r_1 < r_{\max}$ is therefore

$$\frac{V_1}{V_{\max}} = 1.003\left\{1 - e^{-[r_1/(0.187\lambda_c)]^2}\right\}. \tag{18}$$

The case of a radial distance of $r_1 = \lambda_c/3$, for example, gives a fractional volume of 0.9609. About 96% of the weighting of the Gaussian smoother thus lies within a radial distance of $\lambda_c/3$ from the estimation location. The exact value for the Parzen weighting determined by numerical integration, rather than the Gaussian weighting derived analytically above, is about 98%, thus verifying the close similarity between the Parzen and Gaussian weighting functions. Since virtually all of the weighting of the Parzen smoother is from data values within a radius of $\lambda_c/3$ it is apparent why the center half of each swath is not strongly contaminated by edge effects with a filter cutoff of $\lambda_c = 50$ km. For the case of 70-km smoothing, however, most of the swath is contaminated by edge effects.

The magnitude and extent of contamination by edge effects are very situation specific. They are most severe when there are features near the edges of the swath that have strong gradients in the across-track dimension. Such is the case for the swaths considered in Fig. 5 that straddle the meandering core of the southward California Current. Edge effects will be less pronounced in more quiescent regions where lateral gradients are weaker such as in the offshore region of the model domain shown in Fig. 3 where submesoscale variability is much less energetic.

The right pairs of swaths in each column in Fig. 5 show the combined effects of sampling errors and residual measurement noise. The latter is manifest as the mottled features in the smoothed error fields that diminish in magnitude with increasing filter cutoff wavelength λ_c. With 30-km smoothing, the total error field is dominated by residual measurement noise for all three variables. For the region considered in Fig. 5, sampling errors from edge effects become larger than

the residual measurement noise with 50-km smoothing. The total error fields for all three variables are almost completely dominated by sampling errors from edge effects with 70-km smoothing.

We emphasize again that the maps in Figs. 4 and 5 were constructed from simulated SWOT data with homogeneous SSH measurement noise with the swath-averaged standard deviation of $\sigma_{2\text{km}} = 1.37$ cm. The errors near the edges of the swaths will be exacerbated by the larger measurement errors toward the swath edges (see Fig. C1) that have not been considered in this study. Edge-effect sampling errors will therefore be larger from actual SWOT data than inferred from the analysis presented here.

6. Summary and conclusions

The Ka-band Radar Interferometer (KaRIn) on the Surface Water and Ocean Topography (SWOT) satellite with a target launch date in November 2022 promises to revolutionize satellite altimetry by providing high-resolution and accurate measurements of SSH across a pair of 50-km swaths separated by a 20-km nadir gap. The primary oceanographic goal of the SWOT mission is to resolve SSH variability on wavelengths longer than about 15 km, which is nearly a factor of 5 better than can presently be achieved from along-track measurements by conventional nadir-viewing altimeters (Xu and Fu 2012), and more than an order of magnitude better than the resolution capability of SSH fields constructed from measurements by multiple nadir-viewing satellite altimeters (Chelton et al. 2011; Ballarotta et al. 2019). An especially exciting aspect of the SWOT mission is that the swath measurements by KaRIn will provide two-dimensional views of instantaneous SSH fields. This offers the first opportunity to obtain satellite-based estimates of instantaneous surface velocity and relative vorticity computed geostrophically from the gridded SSH measurements across the two parallel measurement swaths.

One of the goals of this study was to determine the standard deviations of the uncorrelated SSH measurement noise for footprint diameters of 0.5, 1, and 2 km (appendix C) from the spectral specification of the science requirement for KaRIn (appendix A), and to quantify the effects of the uncorrelated SSH measurement errors on the noise in geostrophically computed velocity and vorticity (appendix D). We did not address the errors in the geostrophic approximation (see, e.g., the discussion in section 3 of C19). Nor did we consider the effects of the long-wavelength measurement errors (see appendix A).

Our analysis also considered only the effects of swath-averaged uncorrelated errors in the SSH measurements for a significant wave height (SWH) of 2 m. We did not account for the increases of the measurement errors toward both edges of each measurement swath or the increase of measurement errors with increasing SWH (see Fig. C1). The conclusions of this study are therefore likely somewhat optimistic assessments of the resolution capabilities of SWOT estimates of SSH, velocity, and vorticity.

The equations in appendixes C–E and sections 3 and 4 for the standard deviations and wavenumber spectral characteristics of the noise in these three variables are all expressed in terms of the SSH standard deviation σ_h that is the fundamental characterization of the uncorrelated SWOT measurement errors for the chosen footprint diameter. They can therefore be applied for any location across the measurement swath and any SWH, based on the corresponding standard deviation of the SSH measurement noise at that location. Moreover, the prelaunch estimates of σ_h derived in appendix C for the three footprint sizes considered in this study can be replaced in the equations in appendixes C–E and sections 3 and 4 with actual values determined after launch from in-orbit data, or with smaller values that may be obtained in the future through improvements in the onboard and ground-based processing of SWOT data.

The analysis in appendix C first considered KaRIn data with the original planned footprint diameter of 1 km on a 1 km × 1 km grid and then considered the recently revised plan for KaRIn data products with footprint diameters of 0.5 km on an oversampled 0.25 km × 0.25 km grid and 2 km on a 2 km × 2 km grid (JPL 2020, 2021). The standard deviations of the SSH estimates with these three footprint diameters were derived from the science requirement for SWOT, which is expressed in a nonconventional form in terms of the wavenumber spectrum after smoothing with a half-power filter cutoff wavelength of 15 km (see appendix A). Because of the large 5.48-cm standard deviation of the SSH measurement noise with the footprint diameter of 0.5 km and the large data volume on the oversampled 0.25 km × 0.25 km grid, the vast majority of users will likely prefer the SWOT data product with a footprint diameter of 2 km on a 2 km × 2 km grid. The noise standard deviation of these SSH estimates are expected to be $\sigma_{2km} = 1.37$ cm if this data product is produced by smoothing the high-resolution SWOT data product with a half-power filter cutoff wavelength of 4 km (see the discussion in appendixes B and C). The smaller footprint size was not considered in our analysis of smoothed simulated SWOT estimates of SSH, velocity, and vorticity in sections 3–5.

The standard deviations of the noise in SWOT estimates of velocity and vorticity computed geostrophically from SSH with the three footprint diameters of 0.5, 1, and 2 km were derived by propagation-of-error analysis in appendix D. The SWOT estimates of SSH, velocity, and vorticity with a chosen footprint diameter are produced by smoothing the raw SWOT data with a half-power filter cutoff wavelength that is twice the footprint diameter. The resulting fields for any choice of footprint diameter are referred to here as "unsmoothed" to distinguish them from the estimates obtained in sections 3–5 with additional two-dimensional smoothing applied in postprocessing. Equations for the wavenumber spectral distributions of the noise variance of unsmoothed SWOT estimates of SSH, velocity, and vorticity are presented in appendix E. The effects of SSH noise are amplified by the finite difference approximations of the derivatives in the Eqs. (D1a) and (D1b) for geostrophically computed velocity and the Eq. (D2b) for vorticity. The amplification of the effects of SSH

measurement noise is much greater for vorticity because it consists of the sum of two terms, both of which involve double differentiation of SSH. Mapping the geostrophically computed surface vorticity field from SWOT data will therefore be much more challenging than mapping the SSH and geostrophically computed surface velocity fields.

As summarized in section 2, the conclusion from the analysis in the appendixes is that the noise in instantaneous maps of all three variables constructed from unsmoothed SWOT data with any of the three footprint diameters considered here will be too large for the SWOT data products to be used directly for most applications. This is acknowledged in the science requirements for KaRIn that are based on smoothing with a half-power filter cutoff wavelength of $\lambda_c = 15$ km to improve the signal-to-noise (S/N) ratio in SWOT estimates of SSH. It was shown in section 3 that the residual noise decreases rapidly with increased smoothing. The noise standard deviations for SSH, velocity components, and vorticity decrease as approximately λ_c^{-1}, λ_c^{-2}, and λ_c^{-3}, respectively (see Fig. 1). Equations for the wavenumber spectral characteristics of the smoothed noise in each of the three variables are presented in section 4.

While smoothing with a half-power filter cutoff wavelength of $\lambda_c = 15$ km may yield an adequate S/N ratio for SSH, the velocity and vorticity computed geostrophically from in-swath SWOT data will likely have to be smoothed with filter cutoff wavelengths of about 30 and 50 km, respectively. Visual assessments of the effects of this smoothing were presented in section 5 from maps of instantaneous estimates of SSH, velocity, and vorticity constructed from simulated SWOT data based on a high-resolution numerical model of the California Current System. This simulated SWOT sampling provides insight into the contamination of smoothed estimates of the three variables from edge effects of the smoothing within the 50-km width of each measurement swath. These edge effects arise from incomplete data within the span of the smoother. They will be compounded by the larger measurement errors toward the swath edges that were not considered here (see Fig. C1). Our assessment of SWOT capabilities may therefore be somewhat optimistic. The measurement noise decreases with increased smoothing but the errors from edge effects worsen. Smoothing of the in-swath data will likely have to be limited to a half-power filter cutoff wavelength of about 50 km. Even then, edge effects will likely be too large except within approximately the center half of each 50-km swath (see Fig. 5). The estimates in this portion of the swath will nonetheless yield important new insight into global mesoscale variability, especially for the smoothed SWOT estimates of vorticity.

The analysis here considered only spatial smoothing of in-swath instantaneous SWOT data to improve the S/N ratio. Intuitively, edge effects and measurement errors can be reduced with space–time smoothing from multiple SWOT overpasses of the region of interest. In practice, however, the space–time sampling pattern of the SWOT orbit is not well suited to reducing the errors by time averaging in regions of energetic and rapidly evolving submesoscale variability. The 21-day exact-repeat orbit consists of two subcycles of about 10 days.

During each 21-day period, the sampling consists of an inter-leaved pattern of measurement swaths in which adjacent swaths are sampled 10 days apart (see Fig. 3d; see also Figs. 21 and 22 of C19 and the related discussion in the text of that paper). This sampling pattern introduces a second source of sampling errors that arises from the unresolved rapid evolution of small-scale features during the 10-day time separation between adjacent swaths. While space–time smoothing will be useful for mapping mesoscale variability in SSH (see section 12 of C19), it is shown in section 8 of C19 that the resolution capabilities of SWOT estimates of velocity and vorticity actually worsen with time averaging because of sampling errors from the unresolved variability, at least for the time averages of 4 and 14 days considered in that study. Mapping of the surface velocity and vorticity fields from SWOT data will likely have to be done with the aid of dynamic interpolation from a data assimilation model, as suggested, for example, by Ubelmann et al. (2015).

The need to smooth SWOT data with a half-power filter cutoff wavelength of 30–50 km for estimates of velocity and vorticity will be disappointing to investigators interested in smaller submesoscale variability. It should be kept in mind that this is much better than the approximate 200-km-resolution limitation of the SSH fields constructed from measurements by multiple nadir-viewing altimeters. SWOT data will undoubtedly provide important new insight into ocean dynamics at the short end of the range of mesoscale variability and the long end of the range of submesoscale variability. It is also noteworthy that recent modeling and observational studies suggest that the variability of SSH from which velocity and vorticity will be computed geostrophically from SWOT data may be dominated by baroclinic tides and internal waves on wavelength scales up to 50 km or more (e.g., Rocha et al. 2016; Qiu et al. 2017, 2018; Callies and Wu 2019). SWOT data will undoubtedly provide new insight into the SSH structures of these ageostrophic processes. It may be challenging to separate baroclinic tides and internal wave variability from some of the geostrophic submesoscale signals of interest. The resolution of these other processes in SWOT data may therefore prove to be comparable to the resolution limitations that are imposed by the measurement noise that was the focus of this study.

Data availability statement. The snapshot SSH field from the model of the California Current System that was analyzed for Fig. E1 and Figs. 2–5 was obtained from Jeroen Mole-maker at the University of California, Los Angeles.

APPENDIX A

The Science Requirements for SWOT Measurement Errors Over Oceans

The errors of SWOT measurements of SSH can be partitioned into a contribution from uncorrelated measurement errors and a contribution from long-wavelength errors attributable to orbit height errors, antenna pointing errors, errors in biases from significant wave height effects, and errors in the corrections for various geophysical effects on the range estimates. Detailed discussions of these long-wavelength errors can be found in the Mission Performance and Error Budget document (JPL 2017a). As specified in the Science Requirements Document (JPL 2018) and various other SWOT documents, the science requirement for the swath-averaged along-track wavenumber spectrum of the long-wavelength errors is

$$S_{red}(l) = 0.0125\, l^{-2} \text{ cm}^2 \text{ cpkm}^{-1}, \text{ for } 1/1000 < l < 1/15 \text{ cpkm,}$$
(A1)

where l is the along-track wavenumber. For reasons discussed below, the SWOT documentation does not specify this "red noise" spectrum for wavenumbers higher than $l = 1/15$ cpkm (i.e., wavelengths shorter than $\lambda = l^{-1} = 15$ km). The spectrum (A1) of long-wavelength errors is shown extrapolated to wavenumbers higher than $l = 1/15$ cpkm by the red dotted line in Fig. A1.

The details of the wavenumber spectrum of uncorrelated measurement errors depend on the smoothing applied to the SWOT interferograms by the onboard processor for the gridded SSH data products that are derived from the interferograms in ground-based processing (see appendix B). The original plan for the gridded SSH data product was to smooth the interferograms to achieve a footprint diameter of 1 km sampled on a $\Delta x \times \Delta y = 1$ km $\times$ 1 km grid (JPL 2017a). The along-track wavenumber spectrum of the uncorrelated measurement errors for a footprint diameter of 1 km is assumed in this study to be constant for all wavenumbers ("white") up to the Nyquist wavenumber $l_N = (2\Delta y)^{-1} = 0.5$ cpkm, as shown by the blue dashed line in Fig. A1 that is derived in appendix C from the science requirements below.

The original plan to generate SSH estimates with a footprint diameter of 1 km has evolved to a new plan to provide SSH estimates with footprint diameters of 0.5 and 2 km (JPL 2020, 2021). The green and purple dashed lines are the white-noise spectra for the footprint diameters of 0.5 and 2 km, which are also derived in appendix C with the assumption that the spectra are white up to the respective Nyquist wavenumbers of 1 and 0.25 cpkm. The fixed grids on which the SSH estimates are to be provided will be geolocated within the nominal measurement swaths of the satellite overpasses of the 21-day exact-repeat orbit of SWOT. For the discussion here, the grid axes will be aligned locally in across-track and along-track coordinates (x and y, respectively).

The goal of the SWOT mission is for KaRIn to resolve SSH on wavelength scales down to 15 km according to the 68th percentile of the distribution of global wavenumber
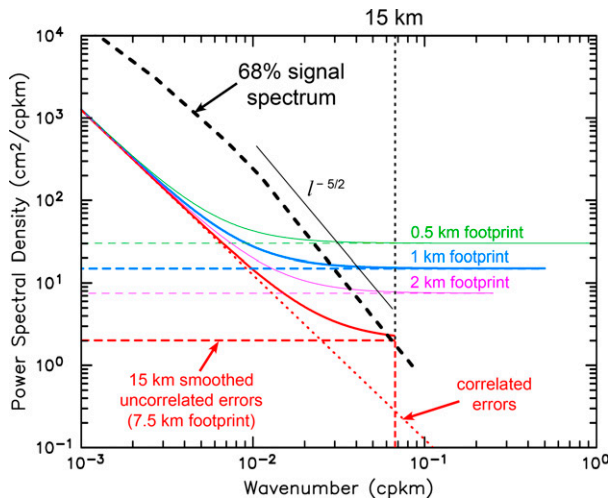
FIG. A1. The swath-averaged along-track wavenumber spectra derived from the science requirements. The dotted red line is the science requirement (A1) for red noise from orbit errors and long-wavelength measurement errors. The dashed red line is the science requirement (A2) for residual uncorrelated errors after smoothing with a half-power filter cutoff wavelength of $\lambda_c = 15$ km. The solid red line is the sum of the spectra of the red noise and the 15-km filtered uncorrelated errors. The dashed blue line is the spectrum (C1) derived in appendix C from (A2) for the uncorrelated errors in SWOT measurements of SSH for a footprint diameter of 1 km without the 15-km smoothing. The solid blue line is the sum of the red noise spectrum and the white noise spectrum for 1-km footprint diameter. The green and purple lines are the analogous spectra of uncorrelated errors and total errors for the footprint diameters of 0.5 and 2 km, shown for wavenumbers up to their associated Nyquist wavenumbers of 1 and 0.25 cpkm for, respectively, the sample grids of 0.5 km × 0.5 km and 2 km × 2 km on which the white noise is uncorrelated for these two footprint diameters. The black dashed line is the 68th-percentile SSH signal power spectral density from JPL (2018).

spectra of SSH inferred from along-track nadir altimeter data that resolve variability down to a wavelength of about 70 km (Xu and Fu 2012). The 68th-percentile spectrum obtained in this manner was extrapolated from 70 km down to the wavelength of 15 km and is shown by the black dashed line in Fig. A1.

The science requirement for the uncorrelated white-noise measurement errors from KaRIn is specified in the SWOT documentation in a nonconventional form in terms of the swath-averaged along-track wavenumber spectrum of residual errors after smoothing in postprocessing with a half-power filter cutoff wavelength of $\lambda_c = 15$ km,

$$\overline{S}_{\text{white}}(l) = 2 \text{ cm}^2 \text{ cpkm}^{-1}, \quad \text{for} \quad 1/1000 \le l \le 1/15 \text{ cpkm.} \quad \text{(A2)}$$

The overbar signifies the 15-km smoothing of the SWOT data. It can be noted that smoothing with a 15-km filter cutoff is effectively equivalent to smoothing to a footprint diameter of 7.5 km.

The residual white-noise spectrum, (A2), after 15-km smoothing of SWOT data, which is shown by the horizontal

red dashed line in Fig. A1, was adopted because it intersects the extrapolated 68th-percentile SSH spectrum at the wavelength of 15 km shown by the vertical red dashed line in Fig. A1. The 15-km smoothing may also be necessary to suppress sources of measurement errors such as wave aliasing and spacecraft vibrations that could result in spectral peaks at wavelengths shorter than 15 km. For the analysis in appendixes C–E and sections 3–5, we take (A2) to be the spectral characterization of the prelaunch estimate of KaRIn SSH measurement noise. The spectrum (A2) could be computed from the SWOT estimates of SSH with 15-km smoothing applied on the swath-based grids for any of the three footprint sizes of 0.5, 1, or 2 km considered in appendix C.

As in the case of the spectrum (A1) of long-wavelength errors, the SWOT documentation does not specify the spectrum (A2) of 15-km smoothed uncorrelated measurement errors for wavenumbers higher than $l_c = \lambda_c^{-1} = 1/15$ cpkm. If the spectrum of the noise without the 15-km smoothing is white up to the Nyquist wavenumbers in both dimensions, and if the 15-km smoothing is applied only one-dimensionally in the across-track dimension, the along-track spectrum of $\overline{S}_{\text{white}}(l)$ would have the value (A2) for all wavenumbers l up to the Nyquist wavenumber, which is 0.5 cpkm for the along-track grid spacing of $\Delta y = 1$ km and a footprint diameter of 1 km in the original plan for the SSH fields generated from SWOT data.

If the 15-km smoothing is applied two-dimensionally with a realizable filter as suggested in section 2.7.2.a of JPL (2018), imperfections of the filter transfer function would result in attenuation but not complete elimination of the along-track spectrum (A2) at high wavenumbers, and there would be a gradual rolloff of attenuation through the half-power filter cutoff wavelength of l_c (see, e.g., the red solid line in the upper-left panel of Fig. 2). Note, however, that subsampling the two-dimensionally smoothed SWOT data with footprint diameters of 0.5, 1, or 2 km at along-track intervals of 7.5 km would yield the truncated error spectrum shown by the red dashed line in Fig. A1 if the spectrum of SSH noise without the 15-km smoothing is white at wavenumbers $l > l_c$, a range that is not explicitly constrained by the spectral characterizations (A1) and (A2) of the science requirements. Subsampling at 7.5-km intervals is not specified in the science requirements for SWOT.

It is evident from the extrapolated spectrum shown by the red dotted line in Fig. A1 that the specification (A1) for long-wavelength measurement errors should have very little power at wavenumbers higher than $l_c = 1/15$ cpkm. Smoothing with a half-power filter cutoff wavelength of $\lambda_c = 15$ km would thus have little effect on the long-wavelength errors. The spectrum of the total measurement errors in 15-km smoothed SWOT data would therefore consist essentially of the sum of the contributions (A1) and (A2), which is shown by the solid red line in Fig. A1. This spectrum of the total errors intersects the 68th percentile of the globally distributed SSH spectra at a wavelength of about 15 km, consistent with the goal of the SWOT mission to achieve a signal-to-noise ratio of 1 at the 15-km wavelength.
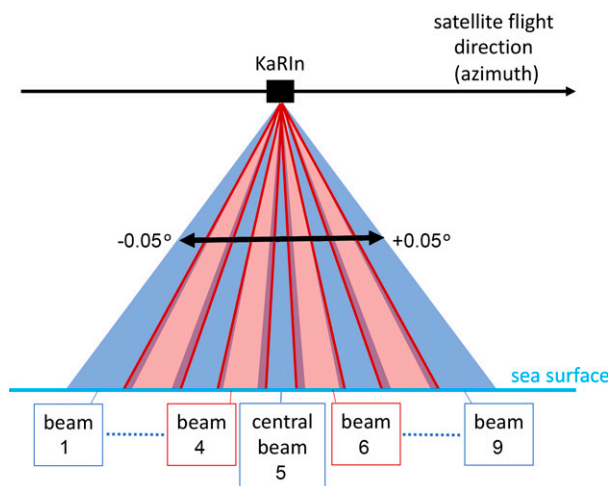
FIG. B1. A schematic depiction of the KaRIn nine-beam measurement geometry, viewed from an across-track perspective. For illustration purposes, the fore-to-aft deflection angles of the squinted beams relative to antenna boresight are shown with the vertical-to-horizontal aspect ratio reduced by about a factor of 300. The alternating blue and pink triangles with slight overlap indicate the nine beams that are measured nearly simultaneously.

This study considers only the contribution of the uncorrelated measurement errors, (A2), to the total errors in KaRIn estimates of SSH and their effects on estimates of velocity and vorticity computed geostrophically from SWOT data. For smoothing with half-power filter cutoff wavelengths longer than about 50 km, comparison of the spectra (A1) and (A2) as in Fig. A1 suggests that additional contributions from the long-wavelength correlated errors may become significant for SWOT estimates of SSH. Because of the high-pass filtering of the derivative operator, correlated SSH measurement errors have a relatively small effect on the SWOT estimates of velocity and vorticity that are the main focus of this study. The contributions of correlated measurement errors are therefore not addressed in this study.

APPENDIX B

An Overview of Onboard and Ground-Based Processing of SWOT Data over Oceans

The KaRIn instrument is a synthetic aperture radar (SAR) that uses interferometry to measure SSH across two 50-km off-nadir swaths with high across-track resolution with SAR processing to achieve approximately equal along-track spatial resolution over the ocean (JPL 2018, 2021). More specifically, KaRIn uses unfocused SAR processing to form nine beams at slightly different squint angles, fanning out from aft to fore in the along-track direction, with along-track effective widths of 500 m and offsets of approximately 130 m on the reflecting sea surface. The angular separation between the fore-most and aft-most beams is approximately 0.1° (Fig. B1). "Unfocused" processing refers to use of a first-order correction for the range to a point on the sea
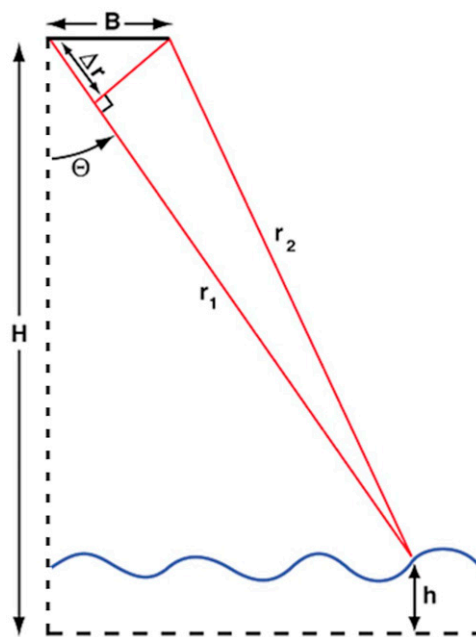

FIG. B2. A schematic description of interferometry. The difference Δr between the pathlengths r_1 and r_2 to a point on the reflecting sea surface can be determined from the phase difference $\phi = 2kr_1 - k(r_1 + r_2) = k(r_1 - r_2)$, where k is the microwave angular wavenumber (equal to 2π divided by the microwave wavelength) of the radar pulses. (After JPL 2017a.)

surface, and hence the Doppler shift of the returned radar pulse, during the time interval required to form the synthetic aperture in the along-track direction. "Squinting" refers to the fore-to-aft spread of the azimuth angles of the synthesized beams formed by the SAR processing. The interferometric baseline is oriented in the across-track direction, which gives sensitivity to the geometric height of the targets viewed by each beam.

For the interferometry, KaRIn uses two antennas separated by a baseline of $B = 10$ m in the across-track direction (Fig. B2). A radar pulse is transmitted from one antenna and the reflected pulse is received by both antennas. The phase difference between the returned radar pulse received by the two antennas at a known look angle θ gives a measure of the difference Δr in the pathlengths between the reflecting target and each of the two antennas. The height h of the sea surface relative to a reference surface is estimated from Δr and the height H of the satellite above the reference surface obtained by precision orbit determination. By processing sequences of returns during short time windows that carry reflections from different distances ("range gating"), resolutions of 10 m at the outer edge of the swath to 70 m at the inner edge can be achieved in the across-track direction. The phase values as a function of range along each swath of each of the nine fore-to-aft beams forms a two-dimensional gridded interferogram in along-track and across-track coordinates (Fig. B3) that is the basis for the KaRIn SSH measurements.
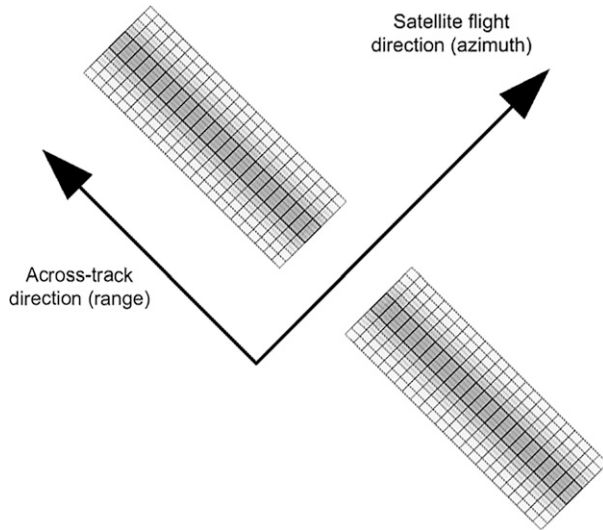
FIG. B3. A plan-view sketch of the nine-beam illumination pattern on the sea surface at a given position of the satellite along the ground track. Pulses along the nine SAR beams illuminate nine partly overlapping across-track swaths with along-track widths of approximately 500 m and offsets of approximately 200 m. Interferometry gives a phase measurement (see Fig. B2) from which SSH is determined with resolution of approximately 500 m in the across-track direction along each of the nine swaths. The closer spacing of the grid lines are intended to depict the oversampling of the across-track interferogram on a 250-m along-track grid rather than at the 500-m across-track spatial resolution of the interferogram. The nadir gap is not shown to scale and only a portion of each across-track swath is shown. (Figure courtesy of Gerald Dibarboure.)

The KaRIn radar transmits with a pulse repetition rate of about 9 kHz, and the onboard processor coherently processes a series of nine pulses at each of the nine beam angles to synthesize the nine fore-to-aft beams, along each of which across-track interferometric measurements are made. Because the nine beams fan out fore to aft, they do not view the same along-track position at a given time (Fig. B1). As the satellite moves along its ground track, however, pulses transmitted along the different beams illuminate a given point on the sea surface at slightly different times (Fig. B4). For the KaRIn instrument and SWOT orbit configuration, pulses along all nine beams illuminate a given across-track swath within a time period of about 0.2 s, thus resulting in nine nearly simultaneous across-track interferograms—one each from pulses at different times along each of the nine beams—at each measurement point along each across-track grid of the interferogram in Fig. B3. The along-track grid points sampled by these nine sets of interferograms are nearly, but not precisely, aligned, with spatial offsets of order 10 m in the along-track direction.

As the satellite moves in the along-track direction, the KaRIn instrument thus collects nine independent, two-dimensional swaths of data, consisting of nine nearly simultaneous across-track interferograms at a sequence of measurement points along the orbit. The natural coordinates for these two-dimensional datasets are azimuth (essentially
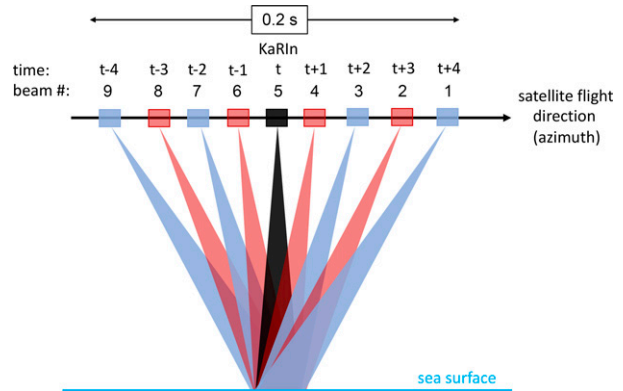

FIG. B4. A schematic depiction of the approximate collocation of nine different beams measured by KaRIn as the satellite moves along its orbit, viewed from an across-track perspective. The time interval required for the nine measurements is approximately 0.2 s. The alternating blue and pink triangles are as in Fig. B1, but measured at nine different times. The center beam is shown as a black triangle. The vertical-to-horizontal aspect ratio has again been reduced by about a factor of 300 for illustration purposes.

along track) and range (essentially across track). The KaRIn onboard processor smooths each of the nine independent interferograms in both the azimuth and range directions with filters that have a half-power filter cutoff wavelength of 1 km, which is the filtering required to achieve a footprint diameter of 0.5 km (see appendix B.1 of C19). As discussed in JPL (2021), a Blackman–Harris smoother will be applied in the azimuth direction and a Parzen smoother will be applied in the range direction.[1] The parameters of both smoothers have been chosen to give the desired half-power filter cutoff wavelength of 1 km in each dimension. It is worth noting that smoothing with different smoothers in each dimension is not isotropic. The smoothed interferograms with a footprint diameter of 0.5 km will be oversampled on a 0.25 km × 0.25 km grid and then telemetered to ground receiving stations along with ancillary data related to spacecraft navigation and signal quality (e.g., the radar backscatter amplitude) in a low-resolution (LR) dataset for oceanographic applications.

---

[1] The rationale given for using a different smoother in each direction in the onboard processing is that the filter transfer function of the Blackman–Harris smoother has slightly better sidelobe suppression than the Parzen smoother (see Fig. 33 of JPL 2021). For technical reasons related to the hardware implementation in the onboard processor, the Blackman–Harris smoother cannot be applied in the range direction. The better sidelobe suppression of the Blackman–Harris smoother is not enough to make any significant, or even detectable, difference in the smoothed interferograms; the largest sidelobe of the filter transfer function of the Parzen smoother is more than 50 dB below the filter transfer function in the pass band (see the aforementioned figure). For all intents and purposes, the two-dimensional smoothing of the interferograms could therefore be achieved equally well by smoothing with a Parzen smoother in both dimensions. This is the form of smoothing used for simulating SWOT data in the present study.

A separate high-resolution dataset is produced for land hydrology using different SAR processing techniques.

In ground-based processing, a number of corrections are made to account for instrumental and geophysical effects. The phase information in the resulting interferograms is then converted to SSH estimates using auxiliary information such as the spacecraft orientation and position and an estimate of the mean sea surface. Using the sampling grid of the central beam as a reference, the SSH estimates from the eight approximately collocated other beams (Fig. B4) are each spatially interpolated to the measurement locations of the central beam using two-dimensional sinc interpolation. At each of the grid points of the central beam, the nine different SSH estimates are then combined using a maximum likelihood estimator (i.e., a weighted average with a weighting that is inversely proportional to the noise; see appendix B of JPL 2021).

The beam-combined SSH estimates with a footprint diameter of 0.5 km are thus obtained on an approximate 0.25 km × 0.25 km grid that is referenced to the ground locations of the central beam of the KaRIn SAR processing, which in turn depends on the spacecraft location and attitude. This native grid of SSH estimates is interpolated (again using two-dimensional sinc interpolation) to a 0.25 km × 0.25 km Earth-fixed grid that is not aligned with the spacecraft ground track.

A coarser-resolution SWOT SSH product that will be used for most oceanographic applications will be formed in ground-based processing by two-dimensional smoothing of the 0.25 km × 0.25 km product on the Earth-fixed grid and subsampling onto a 2 km × 2 km Earth-fixed grid. The details of this final smoothing have not yet been decided by the SWOT Project Office, but it will have a half-power filter cutoff wavelength of at least 4 km.

The net filtering and effective resolution of the SWOT data products on the 0.25 km × 0.25 km and 2 km × 2 km grids are thus determined by the accumulation of the processing steps summarized above, which include smoothing of interferograms by the onboard processor, interpolation of eight of the nine smoothed SSH estimates to a common sampling grid, weighted averaging of those estimates at each of the interpolated grid points, a second interpolation to an Earth-fixed 0.25 km × 0.25 km grid. These SSH fields will subsequently be smoothing in ground-based processing to produce the 2 km × 2 km gridded SSH product.

The net filtering of the SSH product on the 2 km × 2 km grid is dominated by the smoothing in the final step of the processing. It is shown in appendixes C–E and sections 4 and 5 that additional filtering will be needed in postprocessing to suppress the effects of uncorrelated measurement errors to achieve the residual noise level that is required for most oceanographic applications of SWOT data. This additional smoothing will ultimately determine the scales of ocean variability that can be resolved by SWOT. The precise details of the smoothing in the ground-based processing to obtain the 2 km × 2 km gridded SSH product are thus of secondary importance. For the analysis in this study, we have adopted a half-power filter cutoff wavelength of 4 km

for the 2 km × 2 km SSH product; the actual value may end up being somewhat larger than 4 km.

APPENDIX C

The Standard Deviations of SWOT Measurement Noise for Three Footprint Diameters

The expression (A2) for the uncorrelated measurement errors in terms of their spectral characteristics after applying 15-km smoothing in postprocessing is an inconvenient characterization of measurement noise for the majority of users. It is preferable to know the spectral characteristics of the uncorrelated measurement errors in the SWOT data without 15-km smoothing in postprocessing. Moreover, a conventional characterization of the uncorrelated measurement errors in terms of the standard deviation σ_h of the noise at the resolution of the footprint diameter of the SWOT data is much more useful in practice than a spectral characterization. The two are simply related by Parseval's theorem, which expresses σ_h^2 as the integral of the spectrum over wavenumber [see Eq. (C2) below]. The spectrum of the errors in SWOT estimates of SSH and the associated standard deviation are derived in appendix F of C19 from the spectral requirement (A2) for the case of a footprint diameter of 1 km sampled on a 1 km × 1 km grid. The procedure is summarized in this section and extended to the cases of footprint diameters of 0.5 and 2 km that are in the new plan for the ground-based processing of SWOT data that is summarized in JPL (2020).

For estimation of the along-track wavenumber spectrum of the noisy SWOT measurements of SSH, smoothing one-dimensionally with a half-power filter cutoff wavelength of λ_c in the across-track dimension x attenuates the along-track wavenumber spectrum of uncorrelated measurement errors at all along-track wavenumbers by the constant factor of c_{λ_c} that depends on the filter transfer function of the smoother according to (9) in section 4. For the filter transfer function of the Parzen smoother used here, this reduces to (12). This attenuation factor is approximately the same for other smoothers when the parameters of the smoother are calibrated to give the same half-power filter cutoff wavelength λ_c.

If the smoothing of the SWOT data is instead applied two-dimensionally and isotropically with an ideal (but unrealizable) filter, the additional along-track smoothing would attenuate the spectrum to zero at along-track wavenumbers between $l_c = 1/15$ cpkm and the Nyquist wavenumber. For a realizable two-dimensional filter, the spectrum of residual errors after smoothing will exhibit the imperfections of a gradual rolloff through the half-power filter cutoff wavenumber l_c, together with the higher-wavenumber sidelobes of the realizable filter. The details of these imperfections of the filter transfer function are particular to the choice of filter. The result for two-dimensional filtering with a Parzen smoother (see appendix A of C19) are shown by the red solid line in the top-left panel of Fig. 2. (The sidelobes of the filter transfer function for the Parzen smoother are too

small to be seen with the dynamic range of the ordinate in this figure—see, for example, Figs. A.1 and B.1 of C19.)

For the footprint diameter of 1 km considered in the two versions of the SWOT Science Requirements Document preceding the current version (JPL 2018) and the two versions of the Onboard Processing and Algorithm Theoretical Basis Document preceding the current version (JPL 2021), and as still specified in the current version of the Mission Performance and Error Budget document (JPL 2017a), the grid spacing between samples with uncorrelated measurement errors is $\Delta x = \Delta y = 1$ km (see appendix B.1 of C19). With the filter cutoff wavelength $\lambda_c = 15$ km of the across-track smoothing in the science requirement specifications for SWOT, the attenuation factor (9) that is given by (12) is $c_{\lambda_c} \approx 1/7.5$. An intuitive explanation for the factor-of-2 difference between c_{λ_c} and λ_c^{-1} is given in the paragraph following (12) in section 4. The swath-averaged white-noise spectrum of uncorrelated SWOT measurement errors obtained from the science requirement (A2) for the case of a footprint diameter of 1 km without 15-km smoothing would thus be a factor of 7.5 times larger than the white-noise spectrum (A2) of the 15-km smoothed SWOT data,

$$S_{1km}(l) = \frac{1}{c_{\lambda_c}} \overline{S}_{white}(l) = \frac{2}{c_{\lambda_c}} \, cm^2 \, cpkm^{-1} = 15 \, cm^2 \, cpkm^{-1}.$$

$$\text{(C1)}$$

The subscript "1km" indicates that (C1) is specific to the case of a footprint diameter of 1 km and the omission of an overbar on the left side of the equation implies that no additional smoothing has been applied to the SWOT data with the 1-km footprint diameter. The white-noise spectrum (C1) of SWOT data with a footprint diameter of 1 km is shown by the blue dashed line in Fig. A1.

If the uncorrelated measurement errors are white at wavenumbers higher than $l_c = 1/15$ cpkm, the in-orbit performance of SWOT can be more easily validated from the spectrum (C1) of SWOT data with 1-km footprint diameter than from the spectrum (A2) that requires 15-km smoothing of SWOT data. Furthermore, the white-noise floor of the total error spectrum for a footprint diameter of 1 km and a grid spacing of $\Delta y = 1$ km (the solid blue line in Fig. A1) extends far beyond the wavenumber $l_c = 1/15$ cpkm to the Nyquist wavenumber of $l_N = 0.5$ cpkm and is thus clearly distinguished from the SSH signal spectrum and the red noise spectrum at the higher wavenumbers.

The variance of the uncorrelated measurement errors in the SWOT estimates of SSH with a footprint diameter of 1 km and without additional smoothing in postprocessing can be obtained by Parseval's theorem that relates the variance σ^2 of a variable to the integral of its spectrum $S(l)$,

$$\sigma^2 = \int_0^{l_N} S(l) \, dl.$$

$$\text{(C2)}$$

For the case of $S(l)$ equal to the constant white-noise spectrum (C1), this reduces to

$$\sigma_{1km}^2 = l_N \, S_{1km}(l) = \frac{S_{1km}(l)}{2\Delta y} = 7.5 \, cm^2.$$

$$\text{(C3a)}$$

For M discretely sampled observations at along-track intervals of Δy, this integral becomes a discrete summation,

$$\sigma_{1km}^2 = \sum_{j=1}^{M/2} S_{1km}(l_j) \Delta l = \frac{M\Delta l}{2} \, S_{1km}(l_j),$$

$$\text{(C3b)}$$

where $l_j = j\Delta l$ and $\Delta l = (M\Delta y)^{-1}$ is the Fourier wavenumber interval. The zero wavenumber is excluded from the sum in (C3b) because it does not contribute to the sample variance. The multiplicative factor on the right side of (C3b) is $M\Delta l/2 = (2\Delta y)^{-1} = l_N$. The right side of (C3b) is therefore the same as the right side of (C3a). The swath-averaged standard deviation of the uncorrelated measurement errors in SWOT data for a footprint diameter of 1 km derived from the science requirement (A2) is the square root of (C3a),

$$\sigma_{1km} = 2.74 \, cm.$$

$$\text{(C4)}$$

As noted above, this measurement noise is uncorrelated on a sample grid spacing of 1 km × 1 km for the 1-km footprint diameter considered here.

The value of 2.74 cm for σ_{1km} cannot be found in any of the present SWOT documents. However, the specification of the white-noise contribution to the total error spectrum in the unnumbered first equation in section 5.1 of JPL (2017a) can be combined with the unnumbered last equation in section 5.1.1 of that document to deduce a value of $\sigma_{1km} = 2.74$ cm. Somewhat smaller values of 2.5 and 2.4 cm are stated without derivation in sections 5.1.3 and 5.4.5, respectively. And a value of 2.7 cm is stated without explanation in Fig. 47 of JPL (2021), albeit with units mislabeled as mm rather than cm. The lower values of 2.5 and 2.4 cm may be the projected best estimates of what will actually be achieved on orbit. Or they may consider only the effects of instrumental errors, neglecting smaller sources of noninstrumental uncorrelated errors such as the effects of spacecraft pointing errors on the signal-to-noise ratio across the measurement swaths. Both explanations have been offered in personal communications by one of us (DBC) with different SWOT Project team members.

The preceding analysis is for the overall average standard deviation of uncorrelated measurement errors across the SWOT measurement swaths for a footprint diameter of 1 km and an SWH of 2 m. In actuality, the errors will be smallest near the middle of each measurement swath and increase toward both edges of the swaths, and will increase monotonically with increasing SWH. The projected estimates of the dependencies of the standard deviation of uncorrelated measurement errors on SWH and across-track swath location x are shown in Fig. C1 for a footprint diameter of 1 km. The corresponding across-track variation of the white-noise along-track wavenumber spectral value of the uncorrelated measurement errors can be determined by inverting (C3a) to obtain $S_{1km}(l, x, SWH) = l_N^{-1} \sigma_{1km}^2(x, SWH)$ based on the measurement
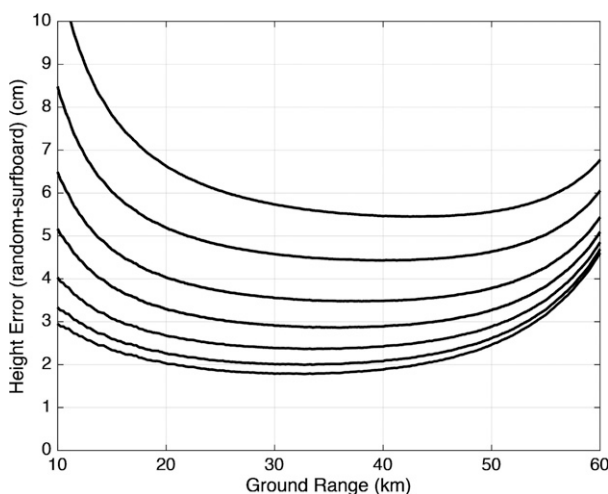
FIG. C1. Estimates of the dependencies of the standard deviation of uncorrelated errors of SWOT measurements of SSH on significant wave height (SWH) and swath location relative to the satellite ground track for a footprint diameter of 1 km. The seven solid lines correspond to SWH values increasing from 2 m (bottom line) to 8 m (top line) at increments of 1 m. The errors for 0-m SWH are essentially the same as those shown for 2-m SWH. The standard deviations of the uncorrelated errors for footprint diameters of 0.5 and 2 km are, respectively, factors of 2 larger and smaller than shown here [see Eqs. (C6) and (C9)]. (Figure adapted from Fig. 2.5 of JPL 2017b.)

error standard deviation $\sigma_{1km}(x, \text{SWH})$ shown in Fig. C1 for the swath location x and SWH of interest.

The discussion hereinafter considers only the across-swath average SSH measurement noise standard deviation for a significant wave height of 2 m. Note, however, that the SWOT simulator software that is provided by the SWOT Project (JPL 2017b) incorporates estimates of both the across-track variation of uncorrelated measurement errors and the additional long wavelength, correlated errors discussed in appendix A.

The original plan for ground-based processing of the SWOT data over the oceans to achieve the footprint diameter of 1 km that was considered above and by C19 has evolved to a new plan to provide the SWOT data with two different footprint sizes (JPL 2020, 2021). As discussed in appendix B, a high-resolution product will be provided with a footprint diameter of 0.5 km on an oversampled 0.25 km × 0.25 km grid. In addition, a coarser resolution product will be produced from the high-resolution product on a 2 km × 2 km grid. As noted in appendix B, the spatial smoothing to be applied for the 2 km × 2 km gridded SSH product has not yet been finalized by the SWOT Project Office. For the analysis presented here, we will assume that this smoothing will be equivalent to a footprint diameter of 2 km. This corresponds to smoothing with a half-power filter cutoff wavelength of 4 km, which is the smoothing for which the residual noise in the 2 km × 2 km gridded estimates of SSH is essentially uncorrelated (see appendix B.1 of C19).

As noted in appendix B, the SWOT Project may smooth with a half-power filter cutoff wavelength somewhat longer than 4 km, thus resulting in 2 km × 2 km gridded estimates of SSH that are oversampled in the sense that the noise is somewhat correlated between neighboring grid points. Since additional smoothing will have to be applied in postprocessing by most users (see sections 3–5), the somewhat greater smoothing that may be applied in the ground-based processing for the 2 km × 2 km gridded SSH product would not significantly alter any of the conclusions of this study.

The noise in SSH estimates with the footprint diameter of 0.5 km is essentially uncorrelated on a sample grid spacing of 0.5 km × 0.5 km. The increased noise of measurement errors with the footprint diameter of 0.5 km compared with a footprint diameter of 1 km is easily determined from the well-known formula that the variance of the average of N uncorrelated measurement errors decreases as $1/N$. Since there are $N = 4$ uncorrelated measurements with 0.5-km footprint in each 1 km × 1 km area, the variance of the uncorrelated errors with a footprint diameter of 0.5 km is 4 times larger than (C3a),

$$\sigma_{0.5km}^2 = 4\,\sigma_{1km}^2 = 30 \text{ cm}^2. \qquad \text{(C5)}$$

The swath-averaged standard deviation of the uncorrelated errors with a footprint diameter of 0.5 km is therefore 2 times larger than (C4),

$$\sigma_{0.5km} = 5.48 \text{ cm}. \qquad \text{(C6)}$$

The recommendation of the SWOT Science Team is to post the high-resolution SSH estimates with the footprint diameter of 0.5 km on an oversampled 0.25 km × 0.25 km grid (JPL 2020). The variance of the SSH measurement errors for the 0.5-km footprint diameter is unchanged on the oversampled grid, but the errors at neighboring 0.25 km × 0.25 km grid points are correlated. The oversampling on a 0.25 km × 0.25 km grid does not alter the wavenumber spectrum of the noise at wavenumbers smaller than the Nyquist wavenumber of $l_N = 1$ cpkm associated with the 0.5 km × 0.5 km grid spacing for uncorrelated errors.

The swath-averaged constant white-noise spectrum of the uncorrelated errors for the smaller footprint diameter of 0.5 km and the higher Nyquist wavenumber of $l_N = 1$ cpkm associated with the grid spacing of $\Delta y = 0.5$ km can be obtained from (C5) by inverting an expression analogous to (C3a) to get

$$S_{0.5km}(l) = \frac{1}{l_N}\,\sigma_{0.5km}^2 = 30 \text{ cm}^2 \text{ cpkm}^{-1}. \qquad \text{(C7)}$$

This spectrum is shown by the green dashed line in Fig. A1. It should be noted that the statistics (C5)–(C7) for the uncorrelated errors in SWOT estimates of SSH with a footprint diameter of 0.5 km are not science requirements for SWOT. The only science requirement for uncorrelated measurement errors is the spectrum (A2) obtained after smoothing the SWOT data one-dimensionally in the across-

track dimension with a half-power filter cutoff wavelength of 15 km in postprocessing.

Because of the large standard deviation (C6) of uncorrelated measurement errors in SSH estimates with a footprint diameter of 0.5 km and the large data volume for SSH fields on the oversampled 0.25 km × 0.25 km grid, the SWOT Project will also provide a lower-resolution and lower-noise product on a 2 km × 2 km grid (JPL 2020). This product will be preferred for most oceanographic applications of SWOT data; as shown in sections 3–5, most users will want to apply additional smoothing. Since there are $N = 16$ measurements with 0.5-km footprint in each 2 km × 2 km grid cell, the variance of the uncorrelated SSH measurement errors with the spatial smoothing equivalent to a footprint diameter of 2 km that is considered here is a factor of 16 smaller than (C5),

$$\sigma^2_{2\text{km}} = \frac{1}{16}\sigma^2_{0.5\text{km}} = 1.875 \text{ cm}^2. \qquad \text{(C8)}$$

This expression can be equivalently derived from (C3a) and the fact that there are $N = 4$ measurements with 1 km footprint in each 2 km × 2 km grid cell, resulting in a variance $\sigma^2_{2\text{km}}$ that is a factor of 4 smaller than (C3a). The swath-averaged standard deviation of the uncorrelated SSH measurement errors with a footprint diameter of 2 km is thus a factor of 4 smaller than (C6) and a factor of 2 smaller than (C4),

$$\sigma_{2\text{km}} = 1.37 \text{ cm}. \qquad \text{(C9)}$$

The standard deviation of the noise in the 2 km × 2 km SSH product will be slightly smaller than this if the half-power filter cutoff wavelength applied to the 0.25 km × 0.25 km SSH product is longer than the value of 4 km assumed in the analysis above.

The swath-averaged constant white-noise spectrum of the uncorrelated errors for the coarser footprint diameter of 2 km and the lower Nyquist wavenumber of $l_N = 0.25$ cpkm associated with the grid spacing of $\Delta y = 2$ km can be obtained from (C8) by again inverting an expression analogous to (C3a) to get

$$S_{2\text{km}}(l) = \frac{1}{l_N}\sigma^2_{2\text{km}} = 7.5 \text{ cm}^2 \text{ cpkm}^{-1}. \qquad \text{(C10)}$$

This spectrum is shown by the purple dashed line in Fig. A1.

The SWOT estimates of SSH with the three footprint diameters of 0.5, 1, and 2 km considered above are produced by smoothing the raw SWOT data with a half-power filter cutoff wavelength that is twice the footprint diameter (see appendix B.1 of C19). The resulting fields for any choice of footprint diameter are referred to throughout this study as "unsmoothed" to distinguish them from the estimates obtained in sections 3–5 with additional two-dimensional smoothing applied in postprocessing.

It was noted above that the in-orbit performance of the uncorrelated errors in KaRIn estimates of SSH can be validated more easily from the spectrum (C1) with a footprint diameter of 1 km and no additional smoothing than it can

from the spectrum (A2) of SSH after 15-km smoothing in postprocessing. The SWOT performance can likewise be easily validated from the spectrum (C7) of gridded SWOT estimates of SSH with a footprint diameter of 0.5 km or from the spectrum (C10) of SWOT data smoothed to have a footprint diameter of 2 km. It will be much easier to evaluate the SWOT performance from unsmoothed SSH observations with any of the three footprint diameters considered above because the white-noise floor of the spectrum of noisy SSH will be more energetic than both the SSH signal spectrum and the spectrum (A1) of long-wavelength measurement errors at wavenumbers higher than the upper limit of $l = 1/15$ cpkm in the science requirement specifications (A1) and (A2). In contrast, the extrapolated 68th-percentile spectrum of SSH with measurement errors and 15-km smoothing does not asymptote to the white-noise floor (A2) of the uncorrelated measurement errors at $l = 1/15$ cpkm. These alternative procedures for evaluating the SWOT performance from data without 15-km smoothing assume that the spectra of the uncorrelated measurement errors are white for all wavenumbers up to the Nyquist wavenumber l_N associated with each of the three footprint diameters considered here.

APPENDIX D

The Standard Deviations of the Noise in SWOT Estimates of Velocity and Vorticity

The discussion of SSH measurement noise in appendix C considered the effects of footprint diameter on the swath-averaged standard deviation of the uncorrelated measurement errors. Many SWOT users will be interested in estimates of surface velocity and vorticity computed geostrophically from the gridded fields of SWOT estimates of SSH. The equations for the x and y components of geostrophic velocity are

$$u_g = -\frac{g}{f}\frac{\partial h}{\partial y}, \qquad \text{(D1a)}$$

$$v_g = \frac{g}{f}\frac{\partial h}{\partial x}, \qquad \text{(D1b)}$$

where h is the SSH, $g = 9.81$ m s^{-2} is the gravitational acceleration, and $f = 2\Omega\sin\theta$ is the Coriolis parameter for Earth rotation rate $\Omega = 7.29 \times 10^{-5}$ s^{-1} and latitude θ. The relative vorticity computed from u_g and v_g or from SSH is

$$\zeta_g = \frac{\partial v_g}{\partial x} - \frac{\partial u_g}{\partial y} \qquad \text{(D2a)}$$

$$= \frac{g}{f}\left(\frac{\partial^2 h}{\partial x^2} + \frac{\partial^2 h}{\partial y^2}\right). \qquad \text{(D2b)}$$

The spatial derivatives in (D1) and (D2) must be estimated from the discretely sampled SWOT estimates of SSH by finite differences. This finite differencing imposes a filtering operation on the SSH fields. The derivative operator for

a continuous variable is a high-pass filter with a wavenumber dependence of k^2 or l^2, depending on whether the derivative is in the x or y dimension, respectively. However, the three-point centered difference operator applied to discretely sampled data, which is the method used to estimate derivatives in this study, is a bandpass filter with a squared response function that has $\sin^2(2\pi k \Delta x)$ or $\sin^2(2\pi l \Delta y)$ dependence on wavenumber k or l [see Eq. (E2) below].

The expressions for the swath-averaged standard deviations σ_{u_g} and σ_{v_g} of the noise of the centered-difference estimates of the geostrophically computed velocity components (D1) and for the standard deviation σ_{ζ_g} of the noise of the centered-difference estimate of the vorticity computed from the first derivatives of u_g and v_g in (D2a) or from the second derivatives of SSH in (D2b) are derived by propagation-of-error analysis in appendix G.1 of C19. The resulting equations are expressed in terms of any specified standard deviation σ_h of the SSH measurement errors and the grid spacings Δx and Δy of the discretely sampled observations. As discussed below, the effects of SSH errors on estimates of u_g and v_g are amplified in the finite differencing of SSH. The effects of these errors are further amplified by the additional finite differencing required to estimate ζ_g from u_g and v_g as in (D1a) or directly from SSH as in (D1b). The equations for σ_{u_g}, σ_{v_g}, σ_{ζ_g} are applied in this section for all three of the footprint diameters of 0.5, 1, and 2 km considered in appendix C.

Consider first the noise in the geostrophically computed velocity component v_g. The propagation of uncorrelated SSH measurement errors through the three-point centered-difference estimates of the geostrophic Eq. (D1b) for v_g yields a noise variance that can be written in the form

$$\sigma_{v_g}^2 = \frac{g^2}{f^2} \frac{2\sigma_h^2}{4\Delta x^2}[1 - \rho_h(2\Delta x)], \tag{D3a}$$

where Δx is the sample interval in the x dimension and $\rho_h(2\Delta x)$ is the autocorrelation of the SSH measurement noise at a spatial lag of $2\Delta x$. This is Eq. (G.2) of C19. When the sample interval Δx is equal to or larger than the footprint diameter, the SSH noise at all grid points is essentially uncorrelated and the term $\rho_h(2\Delta x)$ inside the square brackets is negligible. This can be seen from the bottom panel of Fig. B1a of C19 for the case of a footprint diameter of 1 km on a 1 km × 1 km grid. For smaller sample interval, the SSH errors at neighboring grid points become correlated so that $\rho_h(2\Delta x)$ is nonzero, albeit small unless Δx is very small.

The nonreduced form of the ratio that multiplies the terms in square brackets in (D3a) reveals the amplification of the effects of SSH measurement noise by the centered differencing alluded to above. The multiplicative factor $(g/f)^2/(4\Delta x^2)$ arises from a combination of the factor g/f in the geostrophic relation (D1b) and the factor $2\Delta x$ in the denominator of the three-point centered difference approximation of the derivative in (D1b). These factors transform the units of squared SSH to units of squared velocity component. The remaining factor $2\sigma_h^2$ in the numerator of (D3a)

shows the well-known fact that finite differencing of two noisy SSH measurements doubles the SSH noise variance. If the SSH field is oversampled by decreasing Δx relative to the footprint diameter, the noise variance $\sigma_{v_g}^2$ increases because of the smaller factor Δx^2 in the denominator of (D3a). This increase is mitigated to a small extent by the autocorrelation $\rho_h(2\Delta x)$ at lag Δx that becomes nonzero and positive when Δx is smaller than the spacing at which the SSH observations are uncorrelated.

In reduced form, (D3a) becomes

$$\sigma_{v_g}^2 = \frac{g^2}{f^2} \frac{1}{2\Delta x^2}[1 - \rho_h(2\Delta x)]\sigma_h^2. \tag{D3b}$$

The analogous expression for the variance of the noise in the geostrophically computed velocity component u_g derived by propagation of the SSH errors through the geostrophic equation, (D1a), is

$$\sigma_{u_g}^2 = \frac{g^2}{f^2} \frac{1}{2\Delta y^2}[1 - \rho_h(2\Delta y)]\sigma_h^2, \tag{D4}$$

where Δy is the sample interval in the y dimension and $\rho_h(2\Delta y)$ is the autocorrelation of the SSH measurement noise at a spatial lag of $2\Delta y$. For a given SSH noise variance σ_h^2, it is apparent from (D3) and (D4) that the noise variances of the geostrophically computed velocity components decrease with increasing Coriolis parameter f, i.e., with increasing latitude.

For the cases of the three footprint diameters of 0.5, 1, and 2 km considered in appendix C with sample grid spacings Δx and Δy that are equal to the footprint diameter, the noise is essentially uncorrelated at the grid spacing so that the lagged autocorrelations $\rho_h(2\Delta x)$ and $\rho_h(2\Delta y)$ in (D3) and (D4) are negligible. The noise variances (D3b) and (D4) for the geostrophically computed velocity components then reduce to

$$\sigma_{v_g}^2 = \frac{g^2}{f^2} \frac{1}{2\Delta x^2} \sigma_h^2, \tag{D5}$$

$$\sigma_{u_g}^2 = \frac{g^2}{f^2} \frac{1}{2\Delta y^2} \sigma_h^2. \tag{D6}$$

For the fourth case of a footprint diameter of 0.5 km and an oversampled grid spacing of $\Delta x \times \Delta y = 0.25$ km × 0.25 km discussed in appendix C, the noise variances for u_g and v_g must use the full Eqs. (D3b) and (D4). For this grid spacing that is half of the footprint diameter, the lagged autocorrelations $\rho_h(2\Delta x)$ and $\rho_h(2\Delta y)$ are only 0.05. The expressions for the noise variances are therefore given approximately by (D5) and (D6), but with Δx and Δy half as large as on the 0.5 km × 0.5 km grid. With the small mitigating factor of 0.05 from the correlations at lags $2\Delta x$ and $2\Delta y$, the noise variances $\sigma_{v_g}^2$ and $\sigma_{u_g}^2$ are slightly less than 4 times larger on the oversampled grid.

The noise standard deviations σ_{v_g} and σ_{u_g} computed from the square roots of the variance expressions (D5) and (D6)

are listed in the fourth column of the top half of Table 1 in section 2. For the purposes of this calculation, we used the Coriolis parameter $f_{37°N} = 8.75 \times 10^{-5}$ s^{-1} at the central latitude 37°N of the domain of the model of the CCS that is used for Fig. E1 below and Figs. 2–5 in the text. The noise standard deviation for latitudes other than 37°N can be determined as explained in the table caption. For all four of the cases of footprint diameter and sampling grid considered in appendix C, the noise of the geostrophically computed velocity components is very large. Even for the coarsest footprint diameter of 2 km, the standard deviation of the noise in each velocity component is more than 0.5 m s^{-1}, which corresponds to a noise of about 0.7 m s^{-1} in speed. For most applications, the geostrophically computed velocity fields will have to be smoothed further to obtain scientifically useful instantaneous estimates of velocity. The effects of smoothing of the u_g and v_g noise are investigated in sections 3–5.

The second-order derivatives of SSH in the form (D2b) of the definition of vorticity are approximated here by a succession of two three-point centered differences.[2] The errors of vorticity ζ_g computed from three-point centered differences of geostrophically computed velocity components u_g and v_g at neighboring grid points are given by Eq. (G.7) of C19. The variance of these vorticity errors is determined from the variances and covariances of the five terms in that equation. The variance $\sigma_{\zeta_g}^2$ as expressed by Eq. (G.8) in appendix G.1 of C19 is specific to the case of SSH observations on the same grid on which the SSH noise is uncorrelated, which was the case of interest in that study. The equation for an arbitrarily specified grid spacing and footprint diameter was not included in appendix G.1 of C19. The general expression is the same as Eq. (G.21) in appendix G.3 of C19 that is derived for the residual noise in smoothed estimates of vorticity, except that the smoothed variances on the left and right sides of that equation are replaced with unsmoothed variances, and the lagged autocorrelations of smoothed SSH are replaced with lagged autocorrelations of unsmoothed SSH. For a uniform grid spacing $\Delta y = \Delta x$, the resulting equation is

$$\sigma_{\zeta_g}^2 = \frac{g^2}{f^2}\frac{1}{(4\Delta x^2)^2}\Big[20 + 4\,\rho_h(4\Delta x) - 32\,\rho_h(2\Delta x)$$
$$+ 8\,\rho_h(2\sqrt{2}\Delta x)\Big]\sigma_h^2, \tag{D7}$$

---

[2] The vorticity is estimated here from three-point centered differences of geostrophically computed velocity components at adjacent grid points, which are themselves estimated as three-point centered differences of SSH at adjacent grid points. This is equivalent to approximating the second derivatives of SSH in (D2b) from stencils that span five adjacent grid points. The velocity components could alternatively be estimated as two-point centered differences at locations half way between adjacent grid points, and the vorticity could then be estimated from 2-point centered differences of these velocity estimates. This is equivalent to approximating the second derivatives of SSH from stencils that span only three adjacent grid points. The noise variance of vorticity estimates is a factor of 4 larger on the three-point spans than on the five-point spans used in this study.

where $\rho_h(2\Delta x)$, $\rho_h(2\sqrt{2}\Delta x)$, and $\rho_h(4\Delta x)$ are the autocorrelations of the SSH measurement noise at spatial lags of $2\Delta x$, $2\sqrt{2}\Delta x$, and $4\Delta x$.

For the cases of the three footprint diameters of 0.5, 1, and 2 km considered in appendix C, and with sample grid spacings Δx and Δy that are equal to the footprint diameter, the autocorrelations at nonzero lags are negligible. The noise variance (D7) of the geostrophically computed vorticity then reduces to Eq. (G.8) of C19, which is

$$\sigma_{\zeta_g}^2 = \frac{g^2}{f^2}\frac{20\sigma_h^2}{(4\Delta x^2)^2} \tag{D8a}$$

$$= \frac{g^2}{f^2}\frac{5}{4\Delta x^4}\,\sigma_h^2. \tag{D8b}$$

For the fourth case of a footprint diameter of 0.5 km and an oversampled grid spacing of 0.25 km × 0.25 km considered in appendix C, the noise variance for ζ_g must use the full Eq. (D7). For this grid spacing that is half of the footprint diameter, the lagged autocorrelations $\rho_h(2\sqrt{2}\Delta x)$ and $\rho_h(4\Delta x)$ are both negligible and $\rho_h(2\Delta x) = 0.05$ as in (D3) and (D4). With this small mitigating factor of 0.05 and the factor-of-2 smaller value of Δx, the variance $\sigma_{\zeta_g}^2$ obtained from (D7) is slightly less than 16 times larger on the oversampled grid than on the 0.5 km × 0.5 km grid.

The amplification of the effects of SSH measurement noise from the sequential three-point centered differences used here to compute the vorticity geostrophically from SSH can be quantified by noting that the multiplicative factor $(g/f)^2/(4\Delta x^2)^2$ in (D7) and in the nonreduced form (D8a) arises from a combination of the factor g/f in the geostrophic relations (D1) and the product of two factors $2\Delta x$ in the denominators of the three-point centered differences approximations of the derivatives in (D1) and (D2a). These factors transform the units of squared SSH to units of squared vorticity. The remaining factor of $20\sigma_h^2$ in the numerators of (D7) and (D8a) shows that the centered differencing and the existence of two terms in the vorticity Eq. (D2b) increase the SSH noise variance by a factor of 20. This large amplification compared with the factor-of-2 amplification of the effects of SSH noise variance in the geostrophically computed velocity components deduced above from (D3a) is because the vorticity at a given grid point is computed from SSH observations in a cross pattern of five grid points [see Eqs. (G.7b) and (G.7c) of C19]. On the grids for which (D8) is applicable, the SSH measurement errors at the five individual grid points are essentially uncorrelated with each other. The SSH measurement error at the central grid point appears four times in the expression for the geostrophically computed vorticity errors, so its contribution to the vorticity noise variance is 16 times the SSH noise variance σ_h^2. Each of the other four grid points contributes σ_h^2, thus resulting in a total vorticity noise variance of $20\sigma_h^2$.

The noise standard deviations σ_{ζ_g} computed from the square roots of the variance expressions (D7) and (D8) are listed in the fifth column of the top half of Table 1 in

section 2, again for the Coriolis parameter $f_{37°N}$ at latitude 37°N. The last column of Table 1 lists the vorticity noise standard deviations normalized by the Coriolis parameter $f_{37°N}$, which is easier to interpret than the noise standard deviation in the units of ζ_g. The noise of ζ_g and ζ_g/f for latitudes other than 37°N can be determined as explained in the table caption.

For all four of the cases of footprint diameter and sampling grid considered in appendix C, the noise of the geostrophically computed vorticity is far too large for the vorticity estimates from any of the SWOT data products to be useful directly. Even for the coarsest footprint diameter of 2 km, the standard deviation of the ζ_g noise is nearly 5 times larger than the planetary vorticity $f_{37°N}$ at 37°N. Additional smoothing of SWOT data will thus be even more imperative for geostrophically computed vorticity than for the geostrophically computed velocity. The effects of smoothing of ζ_g noise are investigated in sections 3–5.

APPENDIX E

The Spectral Characteristics of the Noise in SWOT Estimates of Velocity and Vorticity

The swath-averaged along-track wavenumber spectral distributions of the noise variances $\sigma_{u_g}^2$, $\sigma_{v_g}^2$, and $\sigma_{\zeta_g}^2$ listed in the top half of Table 1 are derived in appendix I.1 of C19. While the variances σ_h^2 of the noise in unsmoothed SWOT estimates of SSH with the three footprint diameters of 0.5, 1, and 2 km considered in appendix C are assumed to be uniformly distributed with respect to wavenumber (white) as shown by the green, blue, and purple dashed lines in Fig. A1, it is shown in this appendix that the corresponding wavenumber spectra of the noise in the unsmoothed geostrophically computed SWOT estimates of the across-track velocity component and the vorticity differ significantly from white.

For the analysis that follows, we define the x and y dimensions as in the previous appendixes to be across track and along track, respectively. Consider first the wavenumber spectrum of the geostrophically computed across-track velocity component u_g for an along-track sample grid spacing of Δy. The along-track spectrum of the noise in SWOT estimates of u_g can be deduced from Eqs. (I.2a) and (I.5) in appendix I.1 of C19, which give

$$S_{u_g}(l) = \frac{g^2}{f^2}\, 4\Delta x \Delta y\, k_{\mathcal{N}}\, \sigma_h^2 \big| W_{3\mathrm{pt}}(l, \Delta y)\big|^2 \qquad (E1a)$$

$$= \frac{g^2}{f^2}\, 2\Delta y \big| W_{3\mathrm{pt}}(l, \Delta y)\big|^2 \sigma_h^2, \qquad (E1b)$$

where

$$W_{3\mathrm{pt}}(l, \Delta y) = \frac{\sin(2\pi l \Delta y)}{\Delta y} = \frac{\sin(\pi l/l_{\mathcal{N}})}{\Delta y} \qquad (E2)$$

is the response function for along-track three-point centered differences (see appendix H of C19) and the variables

$k_{\mathcal{N}} = (2\Delta x)^{-1}$ and $l_{\mathcal{N}} = (2\Delta y)^{-1}$ in (E1a) and (E2), respectively, are the Nyquist wavenumbers in the across-track and along-track dimensions. Equations (E1) and (E2) are valid for any specified grid spacings Δx and Δy. Because of the presence of $W_{3\mathrm{pt}}(l, \Delta y)$ on the right sides of (E1a) and (E1b), the wavenumber spectrum of u_g noise deviates dramatically from white (see Fig. E1 below).

The along-track wavenumber spectrum of noise in the geostrophically computed along-track velocity component v_g for an across-track sample grid spacing of Δx is given by Eq. (I.8a) in appendix I.1 of C19, which is

$$S_{v_g}(l) = \frac{g^2}{f^2}\, 4\Delta x \Delta y\, \sigma_h^2 \int_0^{k_{\mathcal{N}}} \big| W_{3\mathrm{pt}}(k, \Delta x)\big|^2 dk, \qquad (E3a)$$

where $W_{3\mathrm{pt}}(k, \Delta x)$ is the response function for across-track three-point centered differences analogous to (E2), but with across-track wavenumber k and grid spacing Δx rather than along-track wavenumber l and grid spacing Δy. The integral on the right side of (E3a) is shown by Eq. (I.9) in appendix I.1 of C19 to be equal to $(4\Delta x^3)^{-1}$. This reduces (E3a) to Eq. (I.10a) of C19, which is

$$S_{v_g}(l) = \frac{g^2}{f^2}\, \frac{\Delta y}{\Delta x^2}\, \sigma_h^2. \qquad (E3b)$$

In contrast to the wavenumber spectrum (E1) of noise in SWOT estimates of u_g, the wavenumber spectrum (E3) of noise in SWOT estimates of v_g is independent of wavenumber l and is therefore white. This is because the derivative in the geostrophic relation (D1b) is orthogonal to the along-track dimension of the spectrum.

The along-track wavenumber spectrum of the noise in SWOT estimates of vorticity computed from three-point centered differences of u_g and v_g is given by Eq. (I.24a) of C19, which is

$$S_{\zeta_g}(l) = \frac{g^2}{f^2}\, 2\Delta y \left[\frac{3}{8\Delta x^4} + \frac{1}{\Delta x^2}\big| W_{3\mathrm{pt}}(l, \Delta y)\big|^2 + \big| W_{3\mathrm{pt}}(l, \Delta y)\big|^4 \right]\sigma_h^2. \qquad (E4)$$

The greater complexity of this equation for the spectrum $S_{\zeta_g}(l)$ of vorticity noise compared with Eqs. (E1b) and (E3) for the spectra $S_{u_g}(l)$ and $S_{v_g}(l)$ of noise in the geostrophically computed velocity components arises from the double differentiation of SSH in (D2b) that is required to compute the noise in ζ_g from the SSH noise, and the fact that the vorticity (D2) consists of a sum of two terms. The wavenumber spectrum of ζ_g noise deviates from white because of the presence of $W_{3\mathrm{pt}}(l, \Delta y)$ in the two terms on the right side of (E4).

A key point to note from (E1), (E3), and (E4) is that the wavenumber spectra of the noise in the derivative variables u_g, v_g, and ζ_g have all been expressed in terms of the SSH noise variance σ_h^2 that is the fundamental characterization of the uncorrelated SWOT measurement errors. The noise spectra for the derivative variables could alternatively be expressed in terms of the white (constant) along-track

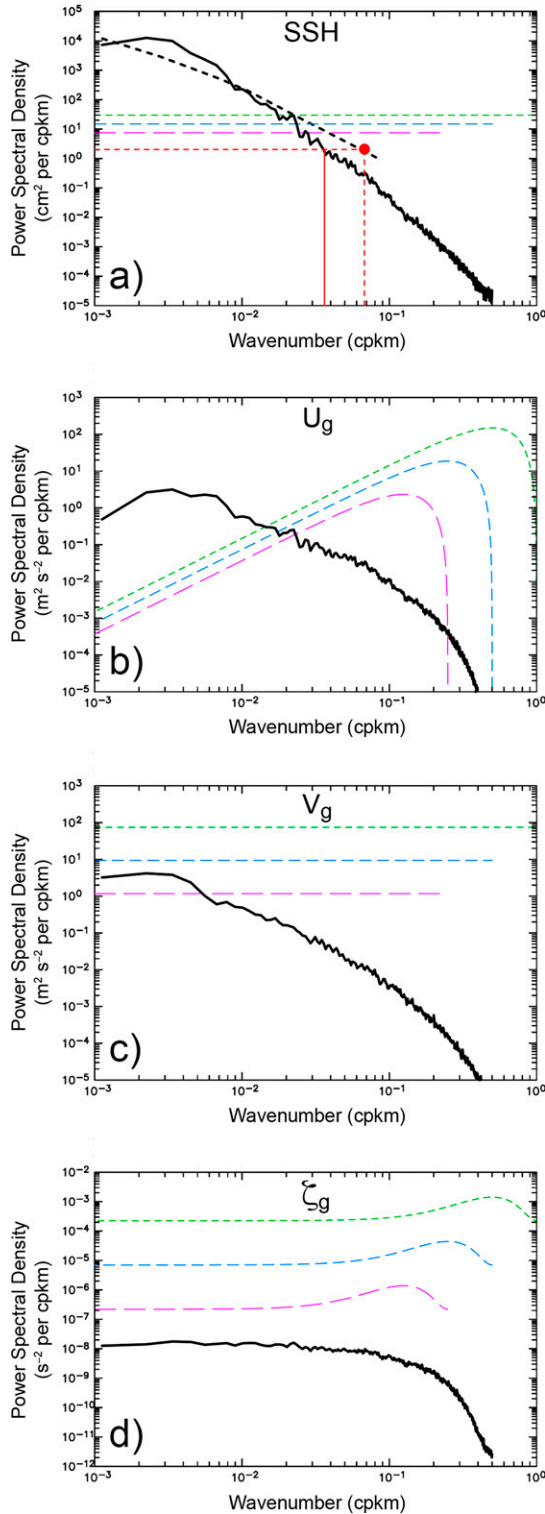## Wavenumber Spectra for 0.5, 1 and 2 km Footprints

FIG. E1. Swath-averaged wavenumber power spectral densities of signals (solid black lines) and noise in SWOT estimates of (a) SSH,

wavenumber spectrum $S_h(l)$ of the SSH measurement noise by Parseval's theorem (C3), (C7), or (C10) that relate σ_h^2 to the integral of the constant white-noise spectrum $S_h(l)$ for footprint diameters of 1, 0.5, and 2 km, respectively.

In the forms (E1b), (E3b), and (E4), the equations for the wavenumber spectra of the noise in SWOT estimates of u_g, v_g, and ζ_g are all valid for any specified σ_h^2 and sample grid spacings Δx and Δy. The spectra for the three footprint diameters of 0.5, 1, and 2 km considered in appendix C can thus be determined by replacing σ_h^2 in (E1), (E3), and (E4) with the prelaunch estimates of $\sigma_{0.5km}^2$, σ_{1km}^2, and σ_{2km}^2 that are given by (C5), (C3), and (C8), respectively. Moreover, these prelaunch estimates can be replaced with the actual values determined after launch from in-orbit data or with smaller values that may be obtained in the future from improvements in the processing of SWOT data.

The along-track wavenumber spectra of noise in u_g, v_g, and ζ_g obtained from (E1b), (E3b), and (E4) for the footprint diameters of 0.5, 1, and 2 km are shown, respectively, by the green, blue, and purple dashed lines in Fig. E1 for the cases of uniform sample grid spacings of $\Delta x = \Delta y$ equal to each of the three footprint diameters. The SSH noise spectra and the 68th percentile of the extrapolated globally distributed SSH spectra in Fig. E1a are the same as in Fig. A1, but with a larger dynamic range of the ordinate to accommodate the solid black line that is the alongshore wavenumber spectrum of error-free SSH computed from a snapshot of the CCS model used in section 5. Note that alongshore for this CCS model corresponds closely to along track for descending overpasses with the inclination of the SWOT orbit (see Fig. 3). The black lines in Figs. E1b–d are the alongshore wavenumber spectra of error-free u_g, v_g, and ζ_g computed from the same snapshot of the CCS model. These signal spectra are included to provide a sense of how the along-track wavenumber distributions of noise variance compare with the wavenumber distributions of the signal

---

(b) u_g, (c) v_g, and (d) ζ_g. The signal spectra were computed in the alongshore dimension from the ROMS model of the California Current System (CCS) considered here for which descending swaths of SWOT are approximately parallel to the coast (see Fig. 3). The black dashed line in (a) is the extrapolated 68% spectrum of SSH from Fig. A1 and the horizontal red dashed line is the science requirement specification (A2) for uncorrelated measurement noise after smoothing with the half-power filter cutoff wavelength of 15 km shown by the vertical red dashed line that intersects the horizontal red dashed line at the red dot. The intersection of the SSH spectrum from the CCS model with the horizontal red dashed line occurs at a wavelength of about 28 km, indicated by the vertical solid red line. The green, blue, and purple dashed lines are, respectively, the noise spectra for each variable for footprint diameters of 0.5 km on a 0.5 km $\times$ 0.5 km grid, 1 km on a 1 km $\times$ 1 km grid, and 2 km on a 2 km $\times$ 2 km grid with the corresponding SSH measurement error standard deviations of $\sigma_{0.5km} = 5.48$ cm, $\sigma_{1km} = 2.74$ cm, and $\sigma_{2km} = 1.37$ cm derived in appendix C. The noise spectra for geostrophically computed velocity components and vorticity are based on the Coriolis parameter of $f_{37°N} = 8.75 \times 10^{-5}$ s^{-1} at the central latitude 37°N of the CCS model.

variance in the CCS region, which may be representative of many regions of the World Ocean.

Before discussing the spectra in Fig. E1, we note a minor caveat to the analytical expressions (E1), (E3), and (E4). These equations require the use of a constant value for the Coriolis parameter f. For the spectra in Figs. E1b–d, we used the value of $f_{37°N} = 8.75 \times 10^{-5}$ s^{-1} for the central latitude of 37°N of the CCS model domain. Over the 32.5°–42°N latitude range of the model, the Coriolis parameter varies by ±11% from $f_{37°N}$. Because f in this latitude range varies approximately linearly with latitude, and because the statistics of the measurement noise are assumed to be homogeneous for the calculations in this study, the latitudinal variation of f is a minor issue. It is shown in Figs. 13 and 14 of C19 that the theoretical noise spectra computed from (E1b), (E3b), and (E4) are essentially identical to the noise spectra computed empirically from simulated SWOT measurement noise in the CCS model.

Consider first the SSH signal and noise spectra in Fig. E1a. To the extent that the CCS model considered here is an accurate representation of reality, this figure raises a concern about whether the goal of resolving SSH variability down to a wavelength of 15 km will be achieved by SWOT. The SWOT documentation adopts a signal-to-noise ratio of 1 as the metric for defining the resolution of SWOT estimates of SSH.[3] As discussed in appendix A, this goal is based on the science requirement (A2) that the along-track wavenumber spectrum of 15-km smoothed SWOT measurement noise intersects the extrapolated 68th percentile of the globally distributed SSH signal spectra at a wavelength of 15 km (see Fig A1). This intersection is indicated by the red dot in Fig. E1a. The along-track wavenumber spectrum of SSH from the CCS model has a steeper rolloff than the 68th-percentile spectrum of SSH. As a consequence, the wavenumber spectrum of smoothed SWOT measurement noise intersects the SSH spectrum from the CCS model at the lower wavenumber of about $l = 0.035$ cpkm shown by the vertical solid red line. This corresponds to a wavelength of about 28 km.

Some of the discrepancy between the 28-km resolution inferred from the CCS model and the 15-km resolution inferred from the extrapolated 68th-percentile spectrum may be attributable to inadequacies in the CCS model. As summarized in section 2 of C19, this model does not include tides and was forced by seasonal cycle winds. The model also has a high dissipation that attenuates internal wave variability. Moreover, the vertical and horizontal grid resolutions are not adequate to resolve the full spectrum of internal waves. It can thus be expected that the model underestimates the variability on scales smaller than about 50 km. However, from the discussion in appendix F of C19

---

[3] For reasons that are discussed in section 5 of C19, a signal-to-noise ratio of 1 is too small for characterization of resolution capability. C19 advocate a signal-to-noise variance ratio of at least 4 and preferably 10 (standard deviation ratios of 2 and 3.16). For the purposes of the present discussion, however, we will discuss resolution in the context of the signal-to-noise ratio of 1 adopted by the SWOT Project.

of the wavenumber spectra from this CCS model and from two versions of a model of the Gulf Stream region (see Figs. F.3 and F.4 of C19), it appears that the inadequacies of the CCS model are not sufficient to explain all of the difference between the 28-km resolution inferred from the CCS model and the 15-km resolution inferred from the 68th percentile of the extrapolated globally distributed SSH spectra.

On the other hand, the 68th-percentile spectrum of SSH is based on nadir altimeter data that resolve SSH only down to wavelengths of about 70 km (Xu and Fu 2012). Little is known observationally about SSH variability on scales shorter than 70 km. The spectra computed from the nadir altimeter data from which the 68th-percentile spectrum was derived were extrapolated from 70 km down to the wavelength of 15 km. Some, and perhaps even much, of the discrepancy between the 28-km resolution inferred from the CCS model and the 15-km resolution inferred from the 68th-percentile spectrum may therefore be attributable to inaccuracies of this extrapolation. Concerns about the validity of the 68th-percentile SSH spectrum at wavelengths shorter than 100 km have been discussed in much greater detail by Callies and Wu (2019). An important contribution of the SWOT mission will be to obtain the first observations of SSH variability at these smaller scales that have not previously been observable from space or in situ data.

The wavenumber spectra of u_g and v_g signal and noise shown in Figs. E1b and E1c differ dramatically. The structure of the wavenumber spectrum of u_g noise is imposed by the fact that the filtering from the three-point centered difference estimate of the derivative in (D1a) is in the same along-track dimension y as the wavenumber spectrum. The u_g noise spectra therefore exhibit the $\sin^2(2\pi l \Delta y)$ structures of the squared response function $|W_{3pt}(l,\Delta y)|^2$ in (E2). (This $\sin^2$ structure is distorted by the logarithmic abscissa in Fig. E1b.) In contrast, the filtering from the three-point centered difference estimate of the derivative in the expression (D1b) for v_g is in the across-track dimension x that is orthogonal to the along-track dimension of the spectrum. It can be seen from (E3a) that the effects of this across-track filtering are integrated in the one-dimensional along-track wavenumber spectra of v_g noise, thus resulting in a constant multiplier on the right side of the equation. The resulting spectra of v_g noise as expressed by (E3b) are constant (i.e., white) and proportional to the value of σ_h^2 that is appropriate for the footprint diameter of interest. If the one-dimensional spectra presented here were in the across-track dimension rather than the along-track dimension, the structures of the spectra of u_g and v_g noise would be reversed. Because of the limited across-track extent of SWOT measurement swaths, across-track spectra cannot be computed directly from SWOT data with the high wavenumber resolution of the along-track spectra in Fig. E1.

It can be seen from Fig. E1b that the spectral power of the across-track velocity component u_g exceeds the noise power for wavenumbers below about 0.02 cpkm (wavelengths longer than 50 km), but this signal variance would be masked in maps or along-track profiles of u_g by the very

energetic noise at higher wavenumbers unless the u_g estimates are smoothed in postprocessing to attenuate this small-scale variability. In the case of the along-track velocity component v_g (Fig. E1c), the spectral power of the v_g noise exceeds the signal power at all wavenumbers for footprint diameters of 0.5 km and 1 km. Without additional smoothing, the v_g signal in the CCS model would therefore be undetectable on any scales in SWOT data with these two footprint sizes. For a larger footprint diameter of 2 km, the v_g noise spectrum exceeds the signal power only at wavenumbers lower than about 0.005 cpkm (wavelengths longer than about 200 km).

The signal and noise spectra for ζ_g are shown in Fig. E1d. The structures of the spectra of ζ_g noise consist of a blend of the structures of the spectra of u_g and v_g noise because the expression (D2) for the geostrophically computed vorticity involves derivatives in both the along-track and the across-track dimensions. The spectral power of the noise far exceeds the signal power for all three footprint diameters. Even for the coarsest footprint diameter of 2 km, the noise power is more than an order of magnitude higher than the signal power at all wavenumbers. Without additional smoothing in postprocessing, the vorticity signal would therefore not be detectable on any scales, even when computed from the SWOT data with a footprint diameter of 2 km.

REFERENCES

Ballarotta, M., and Coauthors, 2019: On the resolutions of ocean altimetry maps. *Ocean Sci.*, **15**, 1091–1109, https://doi.org/10.5194/os-15-1091-2019.

Callies, J., and W. Wu, 2019: Some expectations for submesoscale sea surface height variance spectra. *J. Phys. Oceanogr.*, **49**, 2271–2289, https://doi.org/10.1175/JPO-D-18-0272.1.

Chelton, D. B., 2019: The wavenumber spectra and standard deviations of uncorrelated errors in SWOT measurements of sea-surface height for various footprint sizes. JPL SWOT Doc., 9 pp., https://swot.jpl.nasa.gov/system/documents/files/2253_2253_Chelton_2019_SWOT_Measurement_Noise_190523.pdf.

——, J. C. Ries, B. J. Haines, L.-L. Fu, and P. S. Callahan, 2001: Satellite altimetry. *Satellite Altimetry and the Earth Sciences: A Handbook of Techniques and Applications*, L.-L. Fu and A. Cazenave, Eds., Academic Press, 1–131.

——, M. G. Schlax, and R. M. Samelson, 2011: Global observations of nonlinear mesoscale eddies. *Prog. Oceanogr.*, **91**, 167–216, https://doi.org/10.1016/j.pocean.2011.01.002.

——, ——, ——, J. T. Farrar, M. J. Molemaker, J. C. McWilliams, and J. Gula, 2019: Prospects for future satellite estimation of small-scale variability of ocean surface velocity and vorticity. *Prog. Oceanogr.*, **173**, 256–350, https://doi.org/10.1016/j.pocean.2018.10.012.

Durand, M., L.-L. Fu, D. P. Lettenmaier, D. E. Alsdorf, E. Rodríguez, and D. Esteban Fernandez, 2010: The Surface Water and Ocean Topography mission: Observing terrestrial surface water and oceanic submesoscale eddies. *Proc. IEEE*, **98**, 766–779, https://doi.org/10.1109/JPROC.2010.2043031.

Fu, L.-L., and E. Rodríguez, 2004: High-resolution measurement of ocean surface topography by radar interferometry for oceanographic and geophysical applications. *The State of the Planet: Frontiers and Challenges in Geophysics*, *Geophys. Monogr.*, Vol. 150, Amer. Geophys. Union, 209–224.

——, and R. Ferrari, 2008: Observing oceanic submesoscale processes from space. *Eos, Trans. Amer. Geophys. Union*, **89**, 488–489, https://doi.org/10.1029/2008EO480003.

——, and C. Ubelmann, 2014: On the transition from profile altimeter to swath altimeter for observing global ocean surface topography. *J. Atmos. Oceanic Technol.*, **31**, 560–568, https://doi.org/10.1175/JTECH-D-13-00109.1.

JPL, 2017a: SWOT Project mission performance and error budget. Jet Propulsion Laboratory Doc. D-79084, revision A, 83 pp.

——, 2017b: SWOT simulator documentation. Jet Propulsion Laboratory Doc., release 2.3.0, 44 pp.

——, 2018: Surface Water and Ocean Topography Mission (SWOT) Project science requirements document. Jet Propulsion Laboratory Doc. D-61923, revision B, 29 pp.

——, 2020: Surface Water and Ocean Topography (SWOT) Project SWOT product description. Jet Propulsion Laboratory Doc. D-56407, revision A (DRAFT), 78 pp.

——, 2021: KaRIn: Ka-Band radar interferometer onboard processor (OBP). Jet Propulsion Laboratory Algorithm Theoretical Basis Doc. D-79130, revision B, 79 pp.

Molemaker, M. J., J. C. McWilliams, and W. K. Dewar, 2015: Submesoscale instability and generation of mesoscale anticyclones near a separation of the California Undercurrent. *J. Phys. Oceanogr.*, **45**, 613–629, https://doi.org/10.1175/JPO-D-13-0225.1.

Pascual, A., Y. Faugere, G. Larnicol, and P.-Y. Le Traon, 2006: Improved description of the ocean mesoscale variability by combining four satellite altimeters. *Geophys. Res. Lett.*, **33**, L02611, https://doi.org/10.1029/2005GL024633.

Qiu, B., T. Nakano, S. Chen, and P. Klein, 2017: Submesoscale transition from geostrophic flows to internal waves in the northwestern Pacific upper ocean. *Nat. Commun.*, **8**, 14055, https://doi.org/10.1038/ncomms14055.

——, S. Chen, P. Klein, J. Wang, H. Torres, L.-L. Fu, and D. Menemenlis, 2018: Seasonality in transition scale from balanced to unbalanced motions in the World Ocean. *J. Phys. Oceanogr.*, **48**, 591–605, https://doi.org/10.1175/JPO-D-17-0169.1.

Rocha, C. B., T. K. Chereskin, S. T. Gille, and D. Menemenlis, 2016: Mesoscale to submesoscale wavenumber spectra in Drake Passage. *J. Phys. Oceanogr.*, **46**, 601–620, https://doi.org/10.1175/JPO-D-15-0087.1.

Schlax, M. G., and D. B. Chelton, 2003: The accuracies of crossover and parallel-track estimates of geostrophic velocities from TOPEX/Poseidon and Jason altimeter data. *J. Atmos. Oceanic Technol.*, **20**, 1196–1211, https://doi.org/10.1175/1520-0426(2003)020<1196:TAOCAP>2.0.CO;2.

Ubelmann, C., P. Klein, and L.-L. Fu, 2015: Dynamic interpolation of sea surface height and potential applications for future high-resolution altimetry mapping. *J. Atmos. Oceanic Technol.*, **32**, 177–184, https://doi.org/10.1175/JTECH-D-14-00152.1.

Xu, Y., and L.-L. Fu, 2012: The effects of altimeter instrument noise on the estimation of the wavenumber spectrum of sea surface height. *J. Phys. Oceanogr.*, **42**, 2229–2233, https://doi.org/10.1175/JPO-D-12-0106.1.

Yu, X., A. L. Ponte, N. Lahaye, Z. Caspar-Cohen and D. Menemenlis, 2021: Geostrophy assessment and momentum balance of the global oceans in a tide- and eddy-resolving model. *J. Geophys. Res. Oceans*, **126**, e2021JC017422, https://doi.org/10.1029/2021JC017422.